An Ultra-Hot Neptune in the Neptune desert

James S. Jenkins,[1,2,*] Matías R. Díaz,[1,2] Nicolás T. Kurtovic,[1] Néstor Espinoza,[3] Jose I. Vines,[1]
Pablo A. Peña Rojas,[1] Rafael Brahm,[4,5] Pascal Torres,[6] Pía Cortés-Zuleta,[1] Maritza G. Soto,[7]
Eric D. Lopez,[8] George W. King,[9,10] Peter J. Wheatley,[9,10] Joshua N. Winn,[11] David R. Ciardi,[12]
George Ricker,[13] Roland Vanderspek,[14] David W. Latham,[15] Sara Seager,[13,16] Jon M. Jenkins,[17]
Charles A. Beichman,[12] Allyson Bieryla,[15] Christopher J. Burke,[13] Jessie L. Christiansen,[12]
Christopher E. Henze,[17] Todd C. Klaus,[17] Sean McCauliff,[17] Mayuko Mori,[18] Norio Narita,[19,20,21,22,23]
Taku Nishiumi,[24] Motohide Tamura,[18,21,22] Jerome Pitogo de Leon,[18] Samuel N. Quinn,[15]
Jesus Noel Villaseñor,[13] Michael Vezie,[13] Jack J. Lissauer,[17] Karen A. Collins,[15] Kevin I. Collins,[25]
Giovanni Isopi,[26] Franco Mallia,[26] Andrea Ercolino,[26] Cristobal Petrovich,[27,28] Andrés Jordán,[4,5]
Jack S. Acton,[29] David J. Armstrong,[9,10] Daniel Bayliss,[9] François Bouchy,[30] Claudia Belardi,[29]
Edward M. Bryant,[9,10] Matthew R. Burleigh,[29] Juan Cabrera,[31] Sarah L. Casewell,[29] Alexander Chaushev,[32]
Benjamin F. Cooke,[9,10] Philipp Eigmüller,[31] Anders Erikson,[31] Emma Foxell,[9,10] Boris T. Gänsicke,[9]
Samuel Gill,[9,10] Edward Gillen,[33,†] Maximilian N. Günther,[13] Michael R. Goad,[29] Matthew J. Hooton,[34]
James A. G. Jackman,[9,10] Tom Louden,[9,10] James McCormac,[9,10] Maximiliano Moyano,[35] Louise D. Nielsen,[30]
Don Pollacco,[9,10] Didier Queloz,[33] Heike Rauer,[31,32,36] Liam Raynard,[29] Alexis M. S. Smith,[31]
Rosanna H. Tilbrook,[29] Ruth Titz-Weider,[31] Oliver Turner,[30] Stéphane Udry,[30] Simon. R. Walker,[9]
Christopher A. Watson,[34] Richard G. West,[9,10] Enric Palle,[23,37] Carl Ziegler,[38] Nicholas Law,[39] and
Andrew W. Mann[39]

[1]*Departamento de Astronoma, Universidad de Chile, Camino El Observatorio 1515, Las Condes, Santiago, Chile*
[2]*Centro de Astrofísica y Tecnologías Afines (CATA), Casilla 36-D, Santiago, Chile*
[3]*Space Telescope Science Institute, 3700 San Martin Drive, Baltimore, MD 21218, USA*
[4]*Facultad de Ingeniería y Ciencias, Universidad Adolfo Ibáñez, Av. Diagonal las Torres 2640, Peñalolén, Santiago, Chile*
[5]*Millennium Institute for Astrophysics, Av. Vicuña Mackenna 4860, 782-0436 Macul, Santiago, Chile*
[6]*Center of Astro-Engineering UC, Pontificia Universidad Católica de Chile, Av. Vicuña Mackenna 4860, 7820436 Macul, Santiago, Chile*
[7]*School of Physics and Astronomy, Queen Mary University of London, 327 Mile End Road, London E1 4NS, UK*
[8]*NASA Goddard Space Flight Center, 8800 Greenbelt Rd, Greenbelt, MD 20771, USA*
[9]*Department of Physics, University of Warwick, Gibbet Hill Road, Coventry CV4 7AL, UK*
[10]*Centre for Exoplanets and Habitability, University of Warwick, Gibbet Hill Road, Coventry CV4 7AL, UK*
[11]*Department of Astrophysical Sciences, Princeton University, 4 Ivy Lane, Princeton, NJ 08544 USA*
[12]*NASA Exoplanet Science Institute/Caltech Pasadena, CA, USA*
[13]*Department of Physics and Kavli Institute for Astrophysics and Space Research, Massachusetts Institute of Technology, Cambridge, MA 02139, USA*
[14]*Royal Observatory of Belgium, Ringlaan 3, B-1180 Brussel, Belgium*
[15]*Center for Astrophysics | Harvard & Smithsonian, 60 Garden Street, Cambridge, MA 02138, USA*
[16]*Department of Earth and Planetary Sciences, Massachusetts Institute of Technology, Cambridge, MA 02139, USA*
[17]*NASA Ames Research Center, Moffett Field, CA, 94035*
[18]*Department of Astronomy, The University of Tokyo, 7-3-1 Hongo, Bunkyo-ku, Tokyo 113-0033, Japan*
[19]*Komaba Institute for Science, The University of Tokyo, 3-8-1 Komaba, Meguro, Tokyo 153-8902, Japan*
[20]*JST, PRESTO, 3-8-1 Komaba, Meguro, Tokyo 153-8902, Japan*
[21]*Astrobiology Center, 2-21-1 Osawa, Mitaka, Tokyo 181-8588, Japan*
[22]*National Astronomical Observatory of Japan, 2-21-1 Osawa, Mitaka, Tokyo 181-8588, Japan*
[23]*Instituto de Astrofísica de Canarias (IAC), 38205 La Laguna, Tenerife, Spain*
[24]*Department of Physics, Kyoto Sangyo University, Motoyama, Kamigamo, Kita-ku, Kyoto, 603-8555 Japan*
[25]*George Mason University, 4400 University Drive, Fairfax, VA, 22030 USA*
[26]*Campo Catino Astronomical Observatory, Regione Lazio, Guarcino (FR), 03010 Italy*
[27]*Canadian Institute for Theoretical Astrophysics, University of Toronto, 60 St George Street, ON M5S 3H8, Canada*
[28]*Centre for Planetary Sciences, Department of Physical & Environmental Sciences, University of Toronto at Scarborough, Toronto, Ontario M1C 1A4, Canada*
[29]*Department of Physics and Astronomy, University of Leicester, University Road, Leicester, LE1 7RH, UK*
[30]*Observatoire de Genève, Université de Genève, 51 Ch. des Maillettes, 1290 Sauverny, Switzerland*
[31]*Institute of Planetary Research, German Aerospace Center, Rutherfordstrasse 2, 12489 Berlin, Germany*
[32]*Center for Astronomy and Astrophysics, TU Berlin, Hardenbergstr. 36, D-10623 Berlin, Germany*
[33]*Astrophysics Group, Cavendish Laboratory, J.J. Thomson Avenue, Cambridge CB3 0HE, UK*

[34] *Astrophysics Research Centre, School of Mathematics and Physics, Queen's University Belfast, BT7 1NN Belfast, UK*

[35] *Instituto de Astronomía, Universidad Católica del Norte, Angamos 0610, 1270709, Antofagasta, Chile*

[36] *Institute of Geological Sciences, FU Berlin, Malteserstr. 74-100, D-12249 Berlin, Germany*

[37] *Departamento de Astrofísica, Universidad de La Laguna (ULL), 38206, La Laguna, Tenerife, Spain*

[38] *Dunlap Institute for Astronomy and Astrophysics, University of Toronto, 50 St. George Street, Toronto, Ontario M5S 3H4, Canada*

[39] *Department of Physics and Astronomy, The University of North Carolina at Chapel Hill, Chapel Hill, NC 27599-3255, USA*

ABSTRACT

About one out of 200 Sun-like stars has a planet with an orbital period shorter than one day: an ultra-short-period planet (Sanchis-Ojeda et al. 2014; Winn et al. 2018). All of the previously known ultra-short-period planets are either hot Jupiters, with sizes above 10 Earth radii ($R_\oplus$), or apparently rocky planets smaller than 2 $R_\oplus$. Such lack of planets of intermediate size (the "hot Neptune desert") has been interpreted as the inability of low-mass planets to retain any hydrogen/helium (H/He) envelope in the face of strong stellar irradiation. Here, we report the discovery of an ultra-short-period planet with a radius of 4.6 $R_\oplus$ and a mass of 29 $M_\oplus$, firmly in the hot Neptune desert. Data from the Transiting Exoplanet Survey Satellite (Ricker et al. 2015) revealed transits of the bright Sun-like star LTT 9779 every 0.79 days. The planet's mean density is similar to that of Neptune, and according to thermal evolution models, it has a H/He-rich envelope constituting $9.0^{+2.7}_{-2.9}\%$ of the total mass. With an equilibrium temperature around 2000 K, it is unclear how this "ultra-hot Neptune" managed to retain such an envelope. Follow-up observations of the planet's atmosphere to better understand its origin and physical nature will be facilitated by the star's brightness ($V_{\mathrm{mag}} = 9.8$).

1. MAIN MANUSCRIPT

Using high precision photometry from Sector 2 of the Transiting Exoplanet Survey Satellite (*TESS*) mission at a cadence of two minutes, a candidate transiting planet was flagged for the star LTT 9779 (Jenkins et al. 2016). The candidate was released as a *TESS* Alert in October 2018, and assigned the TESS Object of Interest (TOI) tagname TOI-193 (TIC183985250). The *TESS* lightcurve was scrutinised prior to its public release. No transit depth variations were apparent, no motion of the stellar image was detected during transits, and no secondary eclipses could be found. Data from the Gaia spacecraft (Gaia Collaboration et al. 2016, 2018) revealed only one background star within the *TESS* photometric aperture, but it is 5 mag fainter than LTT 9779 and hence cannot be the source of the transit-like signals, and no significant excess scatter was witnessed in the Gaia measurements. The lack of all these abnormalities supported the initial interpretation that the transit signals are due to a planet with an orbital period of 19 hours and a radius of 3.96 $R_\oplus$.

We also observed four complete transits with ground-based facilities: three with the Las Cumbres Observatory (LCO) and one with the Next Generation Transit Survey (NGTS; Wheatley et al. 2018) telescopes. The LCO and NGTS data have a similar precision to the *TESS* light curve and much better angular resolution. The observed transit depths were in agreement with the depth observed with *TESS*. High-angular resolution imaging of LTT 9779 was performed with adaptive optics in the near-infrared using NIRC2 at the Keck Observatory, and with speckle imaging in the optical using HRCam on SOAR at the Cerro-Tololo Inter-American Observatory. No companions were detected within a radius of $3''$ down to a contrast level of 7.5 magnitudes, and no bright close binary was seen with a resolution of $0.05''$ (see the SI). These observations sharply reduce the possibility that an unresolved background star is the source of the transits. We also tested the probability of having background or foreground stars within a region of $0.1''$ separation (AO limit) from the star, using a Besançon (Robin et al. 2003) model of the galaxy. The model indicates we can expect over 2200 stars in a 1 square degree field around LTT 9779 providing a probability of only 0.0005% of having a star down to a magnitude limit of 21 in V contaminating the lightcurves. If we consider only objects bright enough to cause contamination of the transit depth that would significantly alter the planet properties, this probability drops even more (see the Supplementary Information (SI) for more details). Furthermore, although there exists a 13.5% probability that LTT 9779 could be part of a binary system that passes within this separation limit, spectral analysis rules out all allowable masses whose contaminant light that would be required to push LTT 9779 b outside of the Neptune desert.

[*] Corresponding author E-mail: `jjenkins@das.uchile.cl`

[†] Winton Fellow

Final confirmation of the planet's existence came from high-cadence radial-velocity observations with the High Accuracy Radial-velocity Planet Searcher (HARPS; Pepe et al. 2000). A sinusoidal radial-velocity (RV) signal was detected with the EMPEROR code (Peña Rojas & Jenkins 2020) independently of the transit data, but with a matching orbital period and phase. No other significant signals were detected, nor were any longer-term trends, ruling out additional massive planets with orbital periods of a few years or less. Likewise, no transit-timing variations were detected (see the SI).

To determine the stellar properties, we combined the Gaia data with spectral information from HARPS, along with other spectra from the Tillinghast Reflector Echelle Spectrograph (TRES; Fűrész et al. 2008) and the Network of Robotic Echelle Spectrographs (NRES; Siverd et al. 2018) and compare the star's observable properties to the outputs from theoretical stellar-evolutionary models (MIST and Y2). We also used our new ARIADNE code to precisely calculate the effective temperature and stellar radius (see SI for more information on these methods). The star was found to have a mass, radius, and age of $1.02^{+0.02}_{-0.03}$ $M_\odot$, 0.949 ± 0.006 $R_\odot$, and $2.0^{+1.3}_{-0.9}$ Gyrs, respectively. The effective temperature and surface gravity are consistent with a main-sequence star slightly cooler than the Sun. The spectra also revealed the star to be approximately twice as metal-rich as the Sun ([Fe/H] = $+0.25\pm0.04$ dex). Table 1 displays all the parameter values.

We utilised the juliet code (Espinoza et al. 2019) to perform a joint analysis of the transit and radial-velocity data (Figure 1). The period, mass, and radius of the planet were found to be 0.792054 ± 0.000014 d, $29.32^{+0.78}_{-0.81}$ $M_\oplus$, and 4.72 ± 0.23 $R_\oplus$, respectively. The orbit is circular to within the limits allowed by the radial-velocity data (the posterior odds ratio is 49:1 in favor of a circular model over an eccentric model).

LTT 9779 b sits in the hot Neptune desert (Mazeh et al. 2016) (Figure 2), providing an opportunity to study the link between short-period gas giants and lower mass super-Earths. The planet's mean density is similar to that of Neptune, and the planet's mass and radius are incompatible with either a pure rock or pure water composition (Figure 3), implying that it possesses a substantial H/He gaseous atmosphere. Using 1-D thermal evolution models from Lopez & Fortney (2014), assuming a silicate and iron core and a solar composition gaseous envelope, we find a planet core mass of $27.9^{+1.2}_{-1.0}$ $M_\oplus$, and an atmospheric mass fraction of $9.0^{+2.7}_{-2.9}\%$. We also tested other planet structures, and even in the limiting case of a non-physical pure water-world, there still exists a significant H/He-rich envelope, at the level of $2.2^{+1.1}_{-1.6}\%$. When combined with the high equilibrium temperature for the planet of 1978 ± 19 K, this makes LTT 9779 b an excellent target for future transmission spectroscopy, secondary eclipse studies, and phase variation analyses. All of the planetary model parameters are in Table 2.

LTT 9779 b is the most highly irradiated Neptune-sized planet yet found. It is firmly in the region of parameter space known as the "evaporation desert" where observations have shown a clear absence of similarly sized planets (Sanchis-Ojeda et al. 2014; Lundkvist et al. 2016), and models of photo-evaporative atmospheric escape predict that such low density gaseous atmospheres should be evaporated on short timescales (Lopez 2017; Owen & Wu 2017). As LTT 9779 b is a mature planet found in this desert, it is a particularly high priority target for transmission spectroscopy at wavelengths that probe low density material escaping from planetary upper atmospheres such as Lyman Alpha (Ehrenreich et al. 2015), FUV metal-lines (Vidal-Madjar et al. 2004), Ca and Fe lines (Casasayas-Barris et al. 2019), and the 1.083 μm Helium line (Nortmann et al. 2018).

An interesting comparison can be made between LTT 9779 b and NGTS-4 b (West et al. 2019), the most similar of all the other known planets. NGTS-4 b is not as hot ($\langle T_{\mathrm{eq}} \rangle^a = 1650\pm400$ K) or short-period ($P = 1.337351\pm0.000008$ d) as LTT 9779 b, has a much higher density of 3.45 g/cm^3, and orbits a metal-poor star ($[M/H] = -0.28 \pm 0.10$ dex). These characteristics may be clues that the two planets formed differently: NGTS-4 b may have formed as a relatively small and dense world, whereas LTT 9779 b started life as a much larger and less dense planet (see Figure 4). Indeed, photoevaporation models posit that the bulk population of ultra-short period planets form by growing to around 3 $M_\oplus$, through the accretion of various amounts of light elements from the proto-planetary disk. The intense radiation from the young star then evaporates these close-in planets over an interval on the order of 10^8 yrs, leaving behind small rocky planets with radii less than 1.5 $R_\oplus$ (Owen & Wu 2017). The more massive population of planets can hold onto the bulk of their envelopes until the star becomes quiescent, leaving behind planets with radii $2-3$ $R_\oplus$. However, these planets are generally found to have orbital periods beyond one day, similar to NGTS-4 b, reaching out to 100 days or so. Ultra-short period planets with these radii are rare, and it may be that since LTT 9779 b likely has a large mass, it can hold onto a high fraction of its atmosphere. It could also have migrated to its current position over a longer dynamical timescale, 10^9 years, not leaving enough time to blow-off a large fraction of its atmosphere by photoevaporation.

Assuming energy-limited atmospheric escape, and adopting the current mass, radius and orbital separation of LTT 9779 b, we estimate mass loss rates of $2 - 8 \times 10^{12}$ g s^{-1} during the saturated phase of X-ray emission (for efficiencies of 525%; Owen & Jackson 2012; Ionov et al. 2018). Assuming the X-ray evolution given by Jackson et al. (2012) and the corresponding extreme-ultraviolet emission by Chadney et al. (2015) and King et al. (2018) we estimate a total mass loss of 29 $M_\oplus$. Considering instead the hydrodynamic calculations by Kubyshkina et al. (2018), this mass loss increases to be greater than the total mass of the planet, and employing the detailed atmospheric escape evolution model of Lopez (2017) suggests that the planet could have had an atmospheric mass fraction of up to $\sim$60% of the total planet mass, or around half that of Saturn ($\sim$44 $M_\oplus$). This means that LTT 9779 b could not have formed in situ with properties close to those we measure here, ruling out such a model. Conversely, adopting an initial planet mass and radius equal to that of Jupiter, we estimate a mass-loss of 5.5×10^{28} g over the current age of the system, which would only be $\sim$3% of the total initial planet mass. Therefore, we can be sure that if the planet began as a Jupiter-mass gas giant, photoevaporation cannot be the sole mechanism that removed most of its atmosphere.

One possible mechanism for atmospheric loss is Roche Lobe Overflow (RLO; Valsecchi et al. 2015). Planets with masses of $\sim$1 $M_{\rm J}$ orbiting solar-mass stars can fill their Roche Lobes for orbital periods approaching 12 hours. For progenitor hot Jupiters with large cores ($\sim$30 $M_\oplus$), the initial migration inwards to the RLO orbit is driven by tidal interaction with the host star. The migration can then reverse as mass is stripped from the planet at a rate of 10^{13}- $- 10^{14}$ g s^{-1} and continues on for a Gyr or so, assuming the escaping material settles in an accretion disk around the star and transfers its angular momentum back to the planet. The planet can migrate outwards, reaching an orbital period of $\sim$0.8 days, before inward migration can resume. Planets with smaller masses undergo later inward migration within the mass loss phase. After the completion of RLO, these planets remain with an atmosphere in the region of $7-10$%, in agreement with that of LTT 9779 b, (assuming the planet is not still currently undergoing RLO). Although these planets terminate with no atmosphere and an orbital period of only 0.3 days after 2.1 Gyrs of evolution, commensurate with the current age of LTT 9779 b, less massive planets terminate with orbital periods longer than more massive ones, and their mass loss period increases also. Although some of these models qualitatively fit the data observed for LTT 9779 b, more work is still required to provide a stronger, more realistic description of the formation history of this system. Finally, such a model is also dependent on the assumption that LTT 9779 b started life as a gas giant planet, which is plausible given the planet's large heavy element abundance, and the fact that metal-rich stars are more commonly found to host gas giant planets than more metal-poor stars (Fischer & Valenti 2005).

Table 1. Stellar properties of LTT 9779

Alternative Names	LTT 9779	
	TIC 183985250	TESS
	HIP 117883	HIPPARCOS
	2MASS J23544020-3737408	2MASS
	TYC 8015-1162-1	TYCHO
Catalogue Data		
RA . . . . (J2000)	23h54m40.60s	TESS
DEC . . . . (J2000)	-37d37m42.18s	TESS
pm^{RA} . . . . (mas yr^{-1})	247.615 ± 0.076	GAIA
pm^{DEC} . . . . (mas yr^{-1})	-69.801 ± 0.062	GAIA
π . . . . (mas)	12.403 ± 0.049	GAIA
Photometric Data		
T . . . . (mag)	9.10 ± 0.02	TESS
B . . . . (mag)	10.55 ± 0.04	TYCHO
V . . . . (mag)	9.76 ± 0.03	TYCHO
G . . . . (mag)	9.6001 ± 0.0003	GAIA
J . . . . (mag)	8.45 ± 0.02	2MASS
H . . . . (mag)	8.15 ± 0.02	2MASS
K_s . . . . (mag)	8.02 ± 0.03	2MASS
WISE1 . . . . (mag)	7.94 ± 0.02	WISE
WISE2 . . . . (mag)	8.02 ± 0.02	WISE
WISE3 . . . . (mag)	8.00 ± 0.02	WISE
Spectroscopic, Photometric, and Derived Properties		
$T_{\rm eff}$ . . . . (K)	5445 ± 84	SPECIES
$\log g$ . . . . (dex)	4.43 ± 0.31	SPECIES
[Fe/H] . . . . (dex)	$+0.25 \pm 0.08$	SPECIES
$v \sin i$ . . . . (km s^{-1})	1.06 ± 0.37	SPECIES
v_{mac} . . . . (km s^{-1})	1.98 ± 0.29	SPECIES
$T_{\rm eff}$ . . . . (K)	5496 ± 80	ZASPE
$\log g$ . . . . (dex)	4.51 ± 0.01	ZASPE
[Fe/H] . . . . (dex)	$+0.24 \pm 0.05$	ZASPE
$v \sin i$ . . . . (km s^{-1})	1.7 ± 0.5	ZASPE
$T_{\rm eff}$ . . . . (K)	5499 ± 50	SPC
$\log g$ . . . . (dex)	4.47 ± 0.10	SPC
[m/H] . . . . (dex)	$+0.31 \pm 0.08$	SPC
$v \sin i$ . . . . (km s^{-1})	2.2 ± 0.5	SPC
$T_{\rm eff}$ . . . . (K)	5443^{+14}_{-13}	ARIADNE
$\log g$ . . . . (dex)	$4.35^{+0.16}_{-0.12}$	ARIADNE
[Fe/H] . . . . (dex)	$+0.27 \pm 0.03$	ARIADNE
$M_\star$ . . . . ($M_\odot$)	$1.03^{+0.03}_{-0.04}$	SPECIES + MIST
$M_\star$ . . . . ($M_\odot$)	$1.00^{+0.02}_{-0.03}$	YY + GAIA
$M_\star$ . . . . ($M_\odot$)	$0.77^{+0.29}_{-0.21}$	ARIADNE
$R_\star$ . . . . ($R_\odot$)	0.95 ± 0.01	SPECIES + MIST
$R_\star$ . . . . ($R_\odot$)	0.92 ± 0.01	GAIA + This work
$R_\star$ . . . . ($R_\odot$)	0.949 ± 0.006	ARIADNE
$L_\star$ . . . . (L$_\odot$)	0.68 ± 0.04	YY + GAIA
$L_\star$ . . . . (L$_\odot$)	0.71 ± 0.01	ARIADNE
M_V . . . . (mag)	5.30 ± 0.07	YY + GAIA

Age ....(Gyr)	$2.1^{+2.2}_{-1.4}$	SPECIES + MIST
Age ....(Gyr)	$1.9^{+1.7}_{-1.2}$	YY + GAIA
$\rho_\star$ ....(g cm^{-3})	$1.81^{+0.06}_{-0.07}$	YY + GAIA
Spectral Type	G7V	This work
$< S_{HARPS} >$	0.148±0.008	This work
$< logR'_{HK,HARPS} >$	-5.10±0.04	This work
$P_{rot,v\sin i}$ (days)	45	This work

Table 2. Transit, orbital, and physical parameters of LTT 9779 b. For the prior descriptions, which are the expected probability distributions for each of the fit parameters, $N(\mu, \sigma)$ represents a normal distribution with mean μ and standard deviation σ, whereas $U(a, b)$ and $J(a, b)$ represent a uniform prior and Jeffrey's prior, both defined between points a and b, respectively (see Methods: Global Modelling for more information).

Parameter	Prior	Value
Light-curve parameters		
P (days)	$N(0.792, 0.1)$	0.7920520 ± 0.0000093
T_0 (days)	$N(2458354.22, 0.1)$	$2458354.21430 \pm 0.00025$
r_1	$U(0, 1)$	$0.9417^{+0.0048}_{-0.0060}$
r_2	$U(0, 1)$	$0.0454^{+0.0022}_{-0.0017}$
$\rho_\star$ (kg/m^3)	$N(1810, 130)$	1758^{+125}_{-121}
$q_{1, TESS}$	$U(0, 1)$	$0.45^{+0.20}_{-0.16}$
$q_{2, TESS}$	$U(0, 1)$	$0.43^{+0.35}_{-0.30}$
$q_{1, NGTS}$	$U(0, 1)$	$0.63^{+0.25}_{-0.32}$
$q_{2, NGTS}$	$U(0, 1)$	$0.55^{+0.31}_{-0.35}$
RV parameters		
K (m s^{-1})	$U(-100, 100)$	$19.65^{+0.43}_{-0.43}$
e	0	0
ω (deg)	90	90
$\gamma_{Coralie}$ (m s^{-1})	$N(0, 100)$	$-5.09^{+2.20}_{-2.20}$
γ_{HARPS} (m s^{-1})	$N(0, 100)$	$-4.40^{+0.30}_{-0.31}$
$\sigma_{Coralie}$ (m s^{-1})	$J(10^{-2}, 100)$	$8.03^{+2.15}_{-1.74}$
σ_{HARPS} (m s^{-1})	$J(10^{-2}, 100)$	$1.43^{+0.28}_{-0.24}$
Derived parameters		
$R_p/R_\star$	$-$	$0.0455^{+0.0022}_{-0.0017}$
$a/R_\star$	$-$	$3.877^{+0.090}_{-0.091}$
i	$-$	76.39 ± 0.43
M_p ($M_\oplus$)	$-$	$29.32^{+0.78}_{-0.81}$ $M_\oplus$
R_p ($R_\oplus$)	$-$	4.72 ± 0.23 $R_\oplus$
$\langle T_{eq} \rangle^a$ (K)	$-$	1978 ± 19
a (AU)	$-$	$0.01679^{+0.00014}_{-0.00012}$
ρ_p (g cm^{-3})	$-$	1.536 ± 0.123

^{a} Equilibrium temperature using equation 4 of
Méndez & Rivera-Valentín (2017) with $A = 0.4$, $\beta = 0.5$, and $\epsilon = 1$.

Correspondence and requests for materials should be addressed to James S. Jenkins (jjenkins@das.uchile.cl).

1.1. *Acknowledgements*

1.2. *Author Contributions*

JSJ led the *TESS* precision radial-velocity follow-up program, selection of the targets, analysis, project coordination, and wrote the bulk of the paper. MD, NT, and RB performed the HARPS radial-velocity observations, PT observed the star with Coralie, and MD analysed the activity data from these sources. NE performed the global modeling, with PCZ performing the TTV analysis, and RB, MGS, and AB performing the stellar characterisation using the spectra and evolutionary models. PAPR worked on the `EMPEROR` code and assisted in fitting the HARPS radial-velocities. EDL created a structure model for the planet, and in addition to GWK and PJW, performed photoevaporation modeling. JNW performed analysis of the system parameters. DRC led the Keck NIRC2 observations and analysis. GR, RV, DWL, SS, and JMJ have been leading the *TESS* project, observations, organisation of the mission, processing of the data, organisation of the working groups, selection of the targets, and dissemination of the data products. CEH, SM, and TK worked on the SPOC data pipeline. CJB was a member of the TOI discovery team. SNQ contributed to TOI vetting, TFOP organization, and TRES spectral analysis. JL and CP helped with the interpretation of the system formation and evolution. KAC contributed to TOI vetting, TFOP organization, and TFOP SG1 ground-based time-series photometry analysis. GI, FM, AE, KIC, MM, NN, TN, and JPL contributed TFOP-SG1 observations. JSA, DJA, DB, FB, CB, EMB, MRB, JC, SLC, AC, BFC, PE, AE, EF, BTG, SG, EG, MNG, MRG, MJH, JAGJ, TL, JM, MM, LDN, DP, DQ, HR, LR, AMSS, RHT, RTW, OT, SU, JIV, SRW, CAW, RGW, PJW, and GWK are part of the NGTS consortium who provided follow-up observations to confirm the planet. EP and JJL helped with the interpretation of the result. CB performed the observations at SOAR and reduced the data, CZ performed the data analysis, and NL and AWM assisted in the survey proposal, analysis, and telescope time acquisition. All authors contributed to the paper.
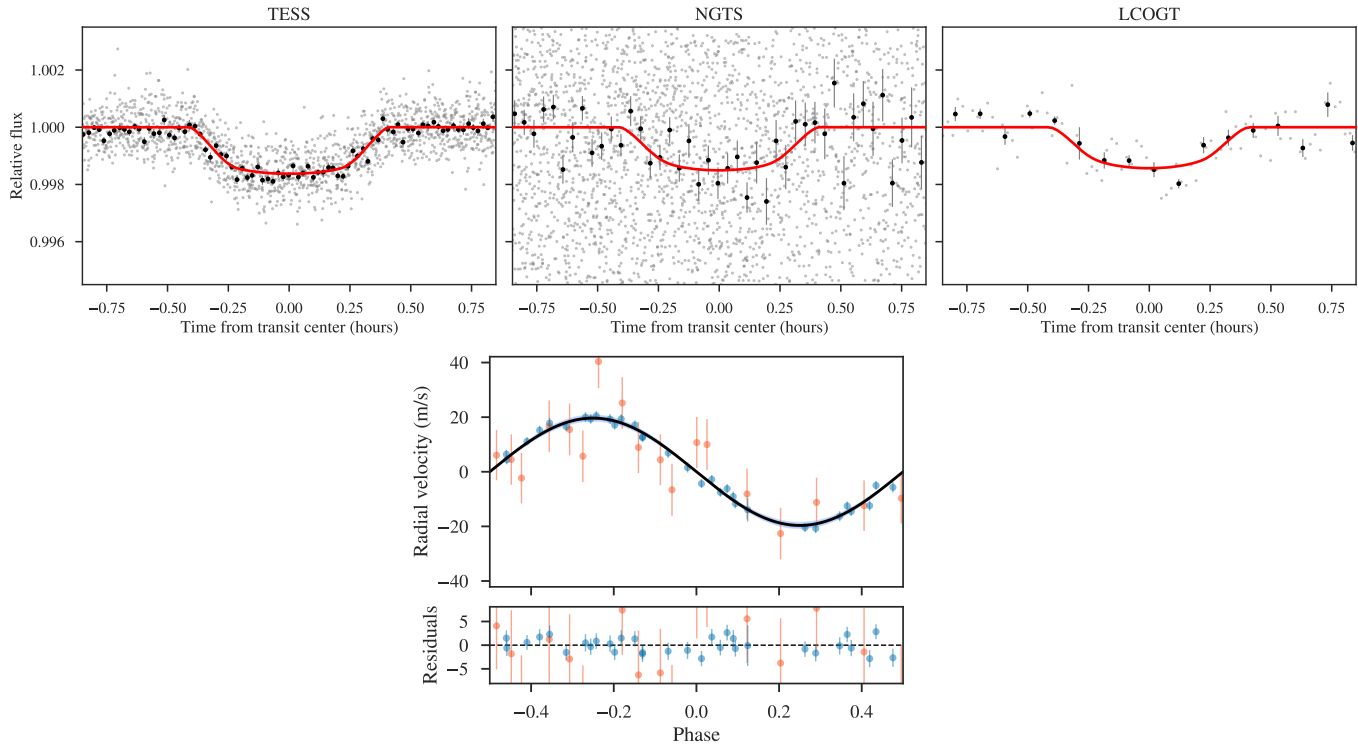
1.3. *Author Information*

Reprints and permissions information is available at `www.nature.com/reprints`. Correspondence and requests for materials should be addressed to James S. Jenkins, `jjenkins@das.uchile.cl`

1.4. *Competing Interests*

The authors declare that they do not have any competing financial interests.

Figure 1. Transit lightcurves and phase folded RVs for LTT 9779 The left top panel shows the discovery *TESS* lightcurve averaging over 33 transits, with the center and right panels showing the single transit follow-up photometry from NGTS and LCOGT for LTT 9779, with a 0.8 day period, and including the associated transit model using the parameters shown in Table 2. The full data set is shown by the small points and the binned data is superimposed on these as the larger and darker points with associated uncertainties. The lower panel shows the 31 HARPS radial-velocities in blue and 18 Coralie measurements in orange (see Table 3), also folded to the period of the planet, and with their respective uncertainties. The mean uncertainty of the Coralie velocities is a factor of 10 larger than those from HARPS. The best fit model is again overplotted on the data. The *TESS* NGTS and LCOGT photometry, along with the HARPS and Coralie velocities were fit simultaneously to ensure the best constraints possible on the planet parameters, along with a more accurate description of the overall uncertainties.

2. EXTENDED DATA
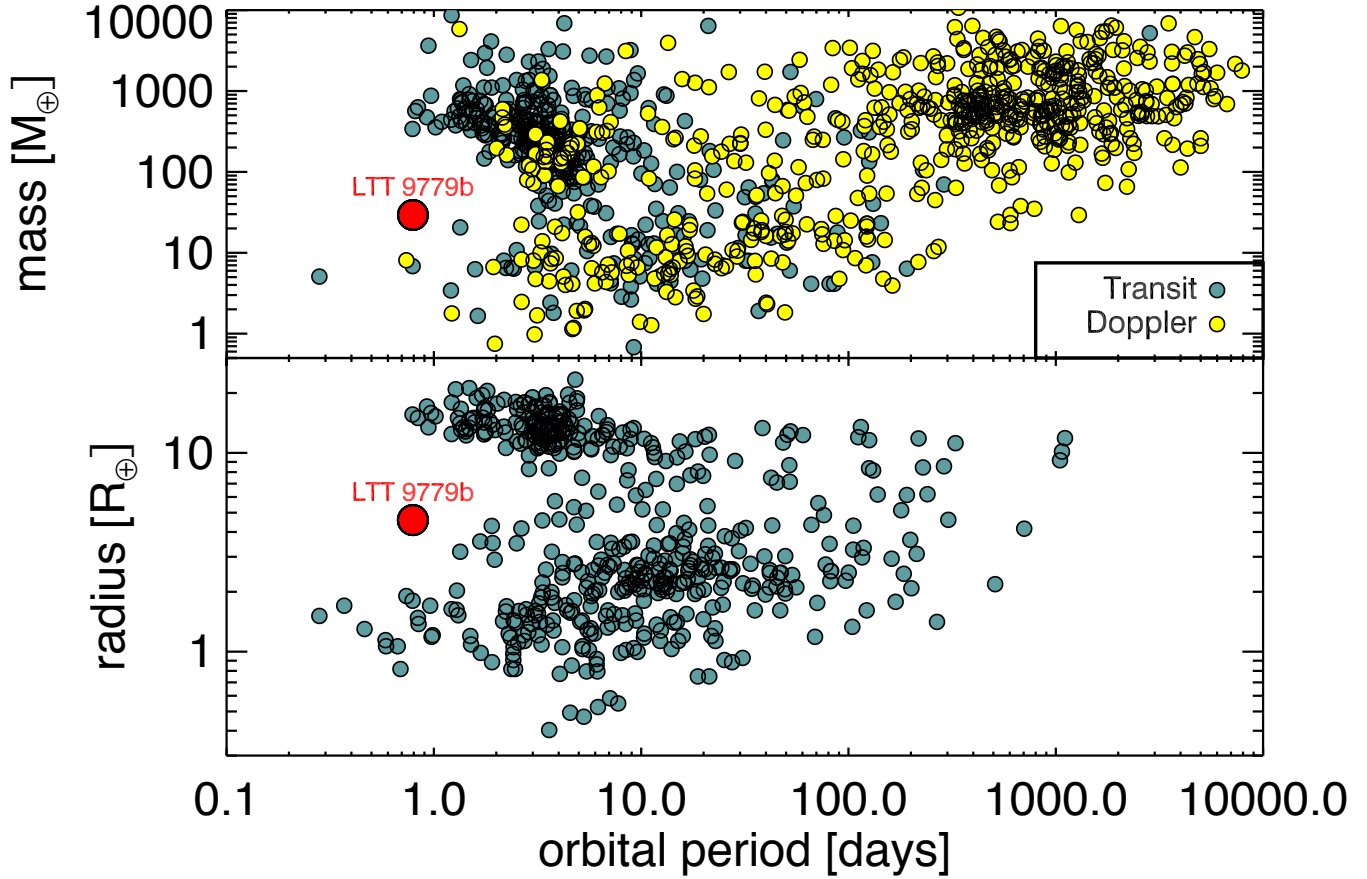
Figure 2. LTT 9779 b in the period-mass and period-radius planes. The top plot shows all currently confirmed planets with a fractional mass uncertainty below 30%, separated in colour by their detection method. The lower plot shows all currently confirmed transit planets with a fractional radius uncertainty below 5%. LTT 9779 b is clearly isolated in the Neptune desert in period-mass-radius space, meaning it is heavily decoupled from the current populations of known exoplanets.
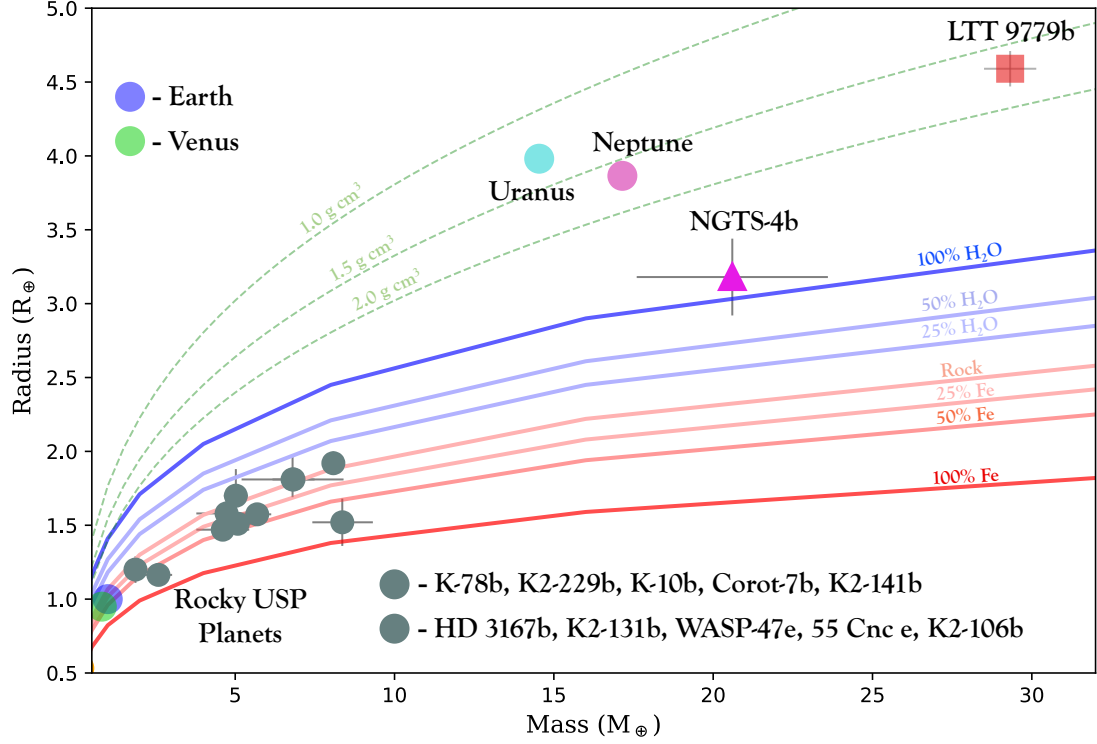
Figure 3. LTT 9779 b in the mass-radius plane. The plot includes all non-gas giant ultra-short period planets with well constrained Doppler masses. LTT 9779 b is marked by the red square. Structure models from Zeng et al. (2016) are plotted as solid curves and labelled depending on the bulk composition of the planet. The models range from a 100% iron core planet, through to a 100% water world. The ultra-short period planets all agree with rocky-iron compositions, explained by photoevaporation of their primordial atmospheres. LTT 9779 b is significantly larger, indicating that it has a residual hydrogen and helium atmosphere around the core. Dashed iso-density curves are shown in green for reference, highlighting the similar densities between Neptune and LTT 9779 b. For reference, Venus, Earth, Uranus, and Neptune are represented in the plot.
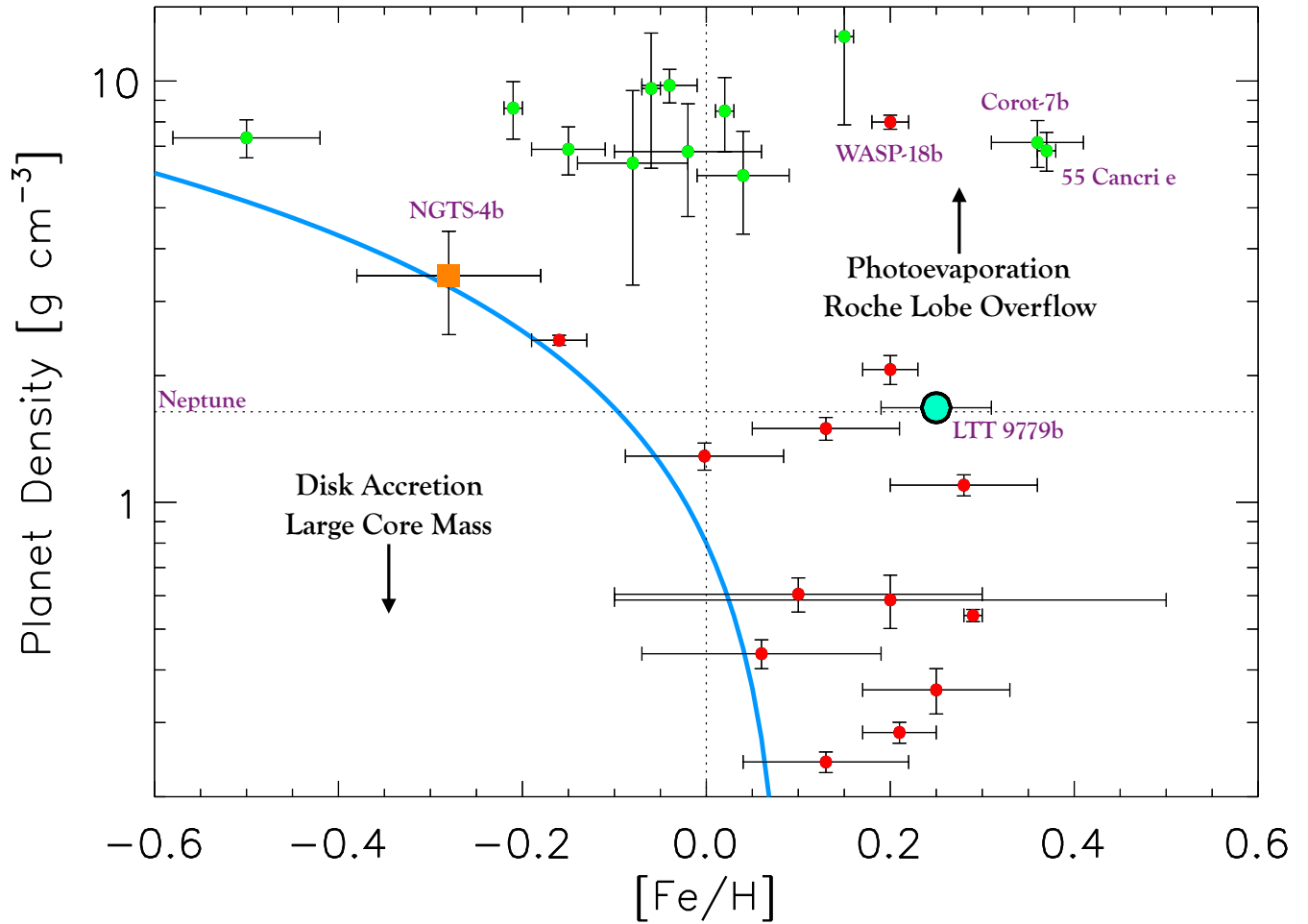
Figure 4. Distribution of planetary densities as a function of host star metallicity for currently known transiting planets with orbital periods less than 1.3 days. The sample is split into those with masses less than $0.1 M_J$ (green circles; ultra-short period planet proxies) and those with masses above (red circles; ultra-hot Jupiter proxies). The ultra-hot Neptune LTT 9779 b and longer period NGTS-4 b are clearly labelled in the figure. The blue curve is a power law described by $3.5 \times [(N_{Fe}/N_H)/(N_{Fe}/N_H)_\odot]^{-2.5} + 0.8$, which bounds the regions governed by the physical processes that determine the planet bulk properties. Those physical processes and the direction in which they move planets are shown in the plot.
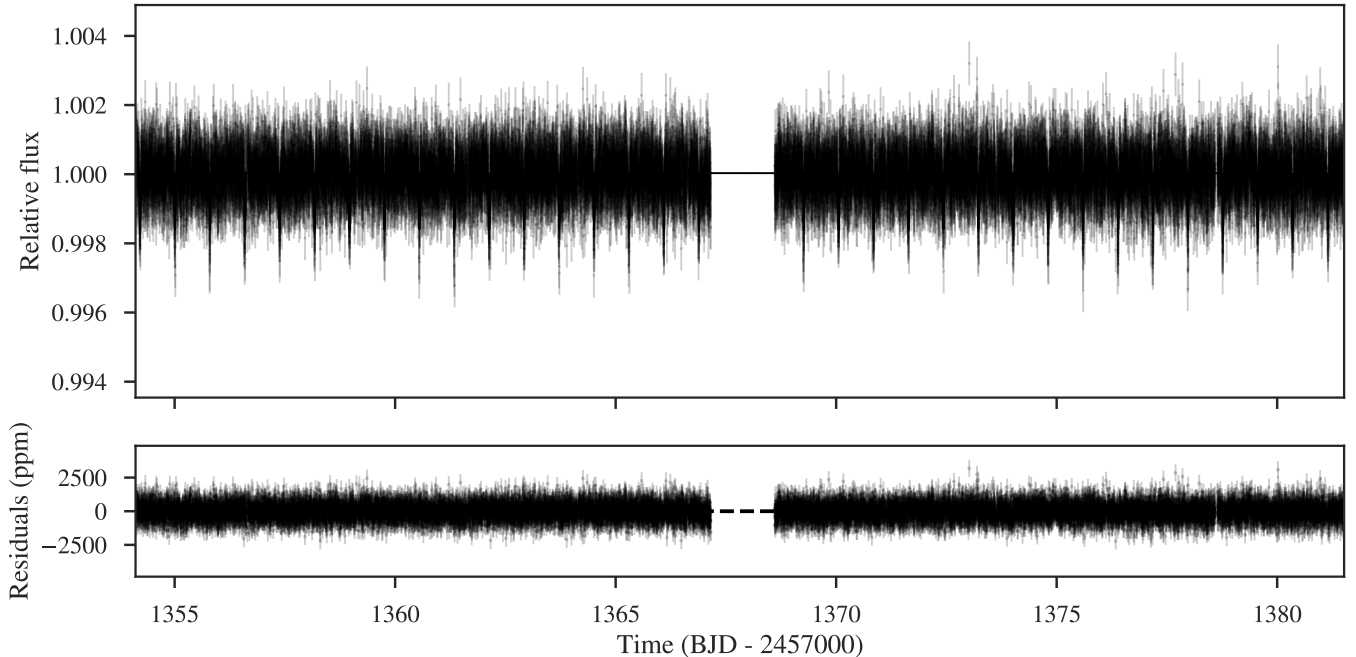
Figure 5. Normalised *TESS* pre-search data conditioning timeseries photometry for LTT 9779 with the optimal model (black curve) overplotted on the data (top). The model residuals are shown in the lower panel.

3. METHODS

TESS Photometry Treatment

TESS observed the star LTT 9779 (HIP 117883, TIC 183985250, TOI 193) using Camera 2 (CCD 4), between UT 2018 Aug 23 and Sep 20 (JD 2458354.11439 − 2458381.51846), part of the Sector 2 observing campaign. The short cadence time sampling of the data was set to two minutes, and data products were then processed on the ground using the Science Processing Operations Center (SPOC) pipeline package (Jenkins et al. 2016), a modified version of the Kepler mission pipeline (Smith et al. 2012; Stumpe et al. 2014; Twicken et al. 2018; Li et al. 2019). SPOC delivers Data Validation Reports to MIT. These reports document so-called "Threshold Crossing Events" identified by the SPOC pipeline, namely dips that could conceivably be due to transiting planets. A team in the TESS Science Office then reviews the reports, including analogous reports from analysis of the Full Frame Images using the Quick-Look Pipeline developed at MIT. There are many criteria that go into deciding whether a TCE is an instrumental artifact or false alarm (e.g. due to low SNR), or an astrophysical false positive due to eclipsing binaries contaminating the TESS photometry or otherwise masquerading as transiting planets. This is the so-called vetting process. Candidates that survive vetting are then assigned TOI numbers and announced to the public, e.g. at MAST, and then work by the TESS Follow-up Observing Program Working Group begins, tracking down TOIs that are not planets but could not be rejected based on the information available to the vetting team. TOIs that survive the reconnaissance work of the TFOP WG can then move on to precision RV work. LTT 9779 b was released as a *TESS* alert on the 4th of October 2018, and assigned the code *TESS* Object of Interest (TOI) 193. As part of the alert process candidate vetting, the light curve modeling did not show any hints of abnormality, such that no transit depth variations were apparent, no PSF centroiding offsets were found, and no secondary eclipses report, giving rise to a bootstrap false alarm probability (FAP) of 2×10^{-278}.

In Figure 5 we show the *TESS* pre-search data conditioning light curve for LTT 9779, after removal of points that were flagged as being affected by excess noise. Given the quiescent nature of the star, the photometric light curve is fairly flat across the full time series, with the small transits (1584 ± 43 ppm) readily apparent to the eye. This simplified the modeling effort, giving rise to the small residual scatter shown in the figure.

Follow-up NGTS Photometry

Photometric follow-up observations of a full transit of LTT 9779 b was obtained on UT 2018 Dec 25 using the Next Generation Transit Survey (NGTS) at ESO's Paranal observatory (Wheatley et al. 2018). We used a new mode of operation in which nine of the twelve individual NGTS telescopes were used to simultaneously monitor LTT 9779 (Smith et al. 2020). We find that the photometric noise is uncorrelated between the nine telescopes, and therefore we improve the photometric precision by a factor of three compared to a single NGTS telescope. The observations were obtained in photometric conditions and at airmass < 2. A total of 6502 images were obtained, each with an exposure time of 10 s using the custom NGTS filter (520−890 nm). The observations were taken with the telescope slightly defocussed to avoid saturation. The telescope guiding was performed using the DONUTS auto-guiding algorithm (McCormac et al. 2013), which resulted in an RMS of the target location on the CCD of only 0.040 pix, or 0.2 ″,. Due to this high precision of the auto-guiding, the use of flat fields during the reduction of the images was not required. Comparison stars were chosen manually and aperture photometry was performed on the images using a custom aperture photometry pipeline. The wide field-of-view provided by NGTS enabled the selection of a good number of suitable comparison stars, despite LTT 9779 being a relatively bright star. When combined, the resulting photometry showed the transit signal of TOI-193 with a depth and transit centre time consistent with the *TESS* photometry. The combined NGTS light curve has a precision of 170 ppm over a half hour timescale, which is a comparable to the *TESS* precision of 160 ppm over this timescale (for a single transit).

Dilution Probability

Given the reality of the transit as 'on-source', the issue of dilution of the light curve by a foreground or background star is considered in a probabilistic sense. In this case, we aim to test the probability of having a blended star so close to the star angularly on the sky, that the AO observations would not have detected it. The AO sensitivity deteriorates quickly below 0.5″ or so, with low sensitivity to objects with angular separations of 0.1″ or less on sky.

3.1. *Background or Foreground Contaminant*

With this in mind, we used the Besançon galactic model (Robin et al. 2003) to generate a representative star field around the position of LTT 9779, with the aim of testing the likelihood of having a diluted star that significantly affects the transit parameters. The model has been used in a similar manner previously. For instance, in Fressin et al. (2013) they applied the model to test the probability that each of the Kepler transit planet candidates in their study was the result of a blended eclipsing binary. We selected all stars within a one square degree box surrounding our target, down to the magnitude limit of $V = 21$ that the model provides. This gave rise to over 2200 stars to work with, for which we randomly assign positions in RA and Dec using a uniform random number generator, constrained to be within the selected box boundaries. We then ran the simulation 10 million times to generate a representative sample, recording all the events where a star passed within a separation of 0.1″ from LTT 9779, and finally normalising by the number of samples probed. The test returned only 48 events, providing a probability to have such a close separation between two stars in this field of only 4.8×10^{-6} (0.0005%).

Although the probability we found is very small, it is actually an upper limit. Blending by stars as faint as 21st magnitude for instance, does not affect the transit depth enough to push the radius of the planet above the Neptune desert. The faintest population of stars in our test, which also represents the most abundant population, biases the probability to larger values. For instance, if we take the mean of the final bin (20.5 magnitudes), we have a magnitude difference from LTT 9779 of 10.2, which relates to an effect at the level of 83 ppm, only 5% of the observed transit depth. If LTT 9779 b is truly a hot Jupiter, then in order to push it out of the Neptune desert, given its orbital period and current radius, we require dilution from a star of ∼5.5 magnitudes or brighter, limiting our test to only stars in magnitude bins of 16 or less. Performing this test decreases further the probability down to 1×10^{-6} (0.00001%), ruling out the possibility that dilution of the light curves is the reason the planet falls in such an isolated part of the parameter space.

3.2. *Binary Star Contaminant*

Although a non-bound stellar contaminant is unlikely to be diluting the transit of LTT 9779 b sufficiently to push it out of the Neptune desert, a binary companion is likely to have a higher chance to be present and tightly separated to LTT 9779. Therefore, we performed Monte Carlo simulations to test how likely having a stellar binary that is bright enough to dilute the transit lightcurve sufficiently would be. We simulated 10^5 binary systems, drawing the system parameters from the probability density functions (PDFs) calculated in Raghavan et al. (2010). Here the

orbital log-period PDF in days is a normal distribution with mean of 5.03 and standard deviation of 2.28. Most other parameters like eccentricity, the orbital angles, and the mass ratio, were simulated using uniform distributions within their respective bounds. Only the system inclinations were drawn from a cosine PDF.

When simulating the systems, we normalized each by the fraction of the orbital period that the secondary star would spend within $0.1''$ of the primary. Therefore, systems that never approached within this angular separation were assigned a fractional time (T_f) of zero, those that always were found within this limit were assigned a value of unity, and the rest were assigned a value between $0-1$ depending on the fractional time spent within this distance. With these calculations we could apply the formulism $P = (\sum_{n=1}^{n=N_t} P_n T_{f,n})/N_t$, where the probability P is the sum total of fractional probabilities $P_n T_{f,n}$ across all samples, normalised by the total number of samples N_t. Finally, we then normalised by the 46% fraction of such stars found to exist in binaries.

With these simulations we arrived at a value of 13.5% for the probability that LTT 9779 has a binary companion that could be found within an angular separation of $0.1''$ at any one time. Although this is a relatively large probability, this is integrated across all binary mass fractions, and therefore does not take into account that only a small mass range is permitted by the spectral analysis. When we account for the cross correlation function analysis discussed below, the probability drops to essentially zero, since the larger secondary masses required to affect the transit depth sufficiently are all ruled out.

Gaia Variability

Another way to probe for very closely separated stars on the sky is to study the measurements made by Gaia, in particular the excess noise parameter ϵ and the Tycho-Gaia astrometric solution (TGAS) discrepancy factor ΔQ (Lindegren et al. 2012; Michalik et al. 2014; Lindegren et al. 2016). These can be used to look for excess variability in the observations that are indicative of blended starlight from a foreground or background star, spatially close enough that they can not be resolved by the instrument.

Both the ϵ and ΔQ parameters are listed in Gaia DR1 as standard outputs, however Gaia DR2 only reports the excess noise, which turns out to be unreliable for stars with G $<\sim$13 (Lindegren et al. 2018). ΔQ measures the difference between the proper motion derived in TGAS and the proper motion derived in the Hipparcos Catalog (van Leeuwen 2007). Also, Rey et al. (2017) utilised both ΔQ and ϵ to show the lack of binarity for some stars. ΔQ is expected to follow a χ^2 distribution with two degrees of freedom for single stars. The Gaia DR1 ϵ and ΔQ for LTT9779 are 0.394 (with a significance of 134.281) and 2.062, respectively. According to Lindegren et al. (2016), all sources obtain a significant excess source noise of $\sim$0.5 mas, due to poor attitude modeling (so an excess noise $>$ 1 - 2 could indicate binarity), and a significance $>$ 2 indicates that the reported excess noise is significant, therefore, from excess noise alone, LTT 9779 is astrometrically well behaved and shows no evidence of binarity. While Michalik et al. (2014) reports a ΔQ threshold of 15.086 for a star to be well behaved (at a significance level of 1%), Lindegren et al. reduces this threshold to 10. This means that any star with $\Delta Q < 10$ is considered to be astrometrically well behaved, again showing that this star is highly likely to be uninfluenced by contaminating light from a background object.

Follow-up Spectroscopy

3.3. NRES Spectroscopy

In order to aid in characterisation of the host star we used the LCO robotic network of telescopes (Brown et al. 2013) and the Robotic Echelle Spectrographs (NRES; Siverd et al. 2018). We obtained 3 spectra, each composed of 3 x 1200 sec exposures, on UT 2018 Nov 5, 8, and 9. All three spectra were obtained with the LCO/NRES instrument mounted on a 1 m telescope at the LCO CTIO node. The data were reduced using the LCO pipeline resulting in spectra with SNR of $61-73$. We have analyzed the spectra using SpecMatch while incorporating the Gaia DR2 parallax using the method described by Fulton & Petigura (2018). The resulting host stars parameters contributed to those listed in Table 1.

3.4. TRES Spectroscopy

We obtained two reconnaissance spectra on the nights of UT2018-11-04 and UT2018-11-05 using the Tillinghast Reflector Echelle Spectrograph (TRES; Fűrész et al. 2008) located at the Fred Lawrence Whipple Observatory (FLWO) in Arizona, USA. TRES has a resolving power of $\sim$44,000, covering a wavelength range of $3900-9100$Å, and the resulting spectra were obtained with SNRs of $\sim$35 at 5200Å. The spectra were then reduced and extracted as described

in Buchhave et al. (2010), whereby the standard processing for echelle spectra of bias subtraction, cosmic ray removal, order-tracing, flatfielding, optimal extraction (Horne 1986), blaze removal, scattered-light subtraction, and wavelength calibration was applied. The Spectral Parameter Classification tool (Buchhave et al. 2012) was used to measure the stellar quantities we show in Table 1.

3.5. *HARPS Spectroscopy*

Upon examination of the light curve we decided to perform high cadence follow-up spectroscopic observations with the High-Accuracy Radial velocity Planet Search spectrograph (HARPS; Pepe et al. 2000) installed at the ESO 3.6m telescope in La Silla, in order to fully cover the phase space. We started observing LTT 9779 on Nov 6th 2018. From an initial visual examination of the spectra and cross correlation function (CCF) of the online Data Reduction Software (DRS), it was consistent with no evidence of blending with other stellar sources nor as being a fast rotator or active, based on the width of the CCF and various activity indicators.

We acquired 32 high-resolution (R$\sim$ 115,000) spectroscopic observations between 2018 Nov 6 and Nov 9, Dec 11 to 13, and Dec 28 to Dec 30, where for the nights of Nov 7,8 and 9th we observed the star four times throughout the night to fully sample the orbital period. We integrated for 1200s, using a simultaneous Thorium-Argon lamp comparison source feeding fiber B, and we achieved a mean signal-to-noise ratio of $\sim$65.4. We then reprocessed the observations using the HARPS-TERRA analysis software (Anglada-Escudé & Butler 2012) where a high-signal to noise template is constructed from all the observed spectra. Then the radial velocities are computed by matching each individual observation to the template, and we list these measurements in Table 3.

HARPS-TERRA receives the observed spectra, stellar coordinates, proper motions, and parallaxes as input parameters. The output it produces then consists of a series of radial velocities that are calculated for a given wavelength range in the echelle. We used the weighted radial-velocities that were calculated starting from the 25th order of the HARPS echellogram, which is centered at a wavelength of 4500 Å. We chose this wavelength range since the uncertainties it produced had the lowest MAD[1] value. This is likely due to increased stellar activity noise that affects the bluest orders the most, combined with relatively low signal-to-noise ratios, and therefore removing these orders allows higher precision to be reached. It was with this data that we performed the EMPEROR (Peña Rojas & Jenkins 2020) fitting, providing the independently confirmed and constrained evidence for LTT 9779 b (Figure 6). For instance, the Doppler orbital period was found to be 0.7920 $\pm$0.0001 d, in excellent agreement with that provided by the TESS transit fitting, and allowing the period to be constrained in the joint fit to one part in 80'000 (0.001%). We also used this spectra to test if possible spectral line asymmetries and/or activity related features could be driving the signal. In particular, we searched for linear correlations between the spectral bisector inverse slope measurements and the radial-velocities (see Figure 7), along with performing period searches using Generalized Lomb Scargle periodograms (Zechmeister & Kürster 2009) and Bayesian methods with the EMPEROR code. The Spearman correlation coefficient between the BIS and RVs is found to be 0.22 with a p-value of 0.22, meaning there exists no strong statistical evidence to reject the null hypothesis that such a weak correlation has arisen by chance. From the periodogram analyses, no statistically significant periodicities were detected with false alarm probabilities of less than 0.1%, our threshold for signal detection. We also performed the same analyses on the full width at half maximum of the HARPS cross-correlation function, and chromospheric activity indicators like the S, Hα, and HeI indices, again with no statistically significant results encountered.

Finally, we also reprocessed the HARPS spectra to generate CCFs with binary masks optimised for spectral types between G2-M4, but across a wider ± 200 km s^{-1} range in velocity to check for weaker secondary CCFs that could be due to additional, nearby companions. We took a typical HARPS LTT 9779 spectrum and injected mid-to-late M star spectra with decreasing SNRs, until we could not detect the M star CCFs no more, providing an upper limit on the mass of any contaminating secondary. From analysis of the mean flux ratio between the M stars and LTT 9779, we found that we should be able to detect stellar contaminants down to a mass of 0.19 $M_\odot$, using the mass-luminosity relation of Benedict et al. (2016), however no companion CCFs were detected. Such a companion would have a magnitude difference of over 7.5, and since we previously calculated above that a maximum magnitude difference of 5.5 would be required to push LTT9779b out of the Neptune Desert, the limits permitted by the CCF analysis show that a diluted companion would not change the conclusions of our work.

[1] Median Absolute Deviation = median($|x_i - median(x)|$)

3.6. *Coralie Spectroscopy*

Additional phase coverage was performed using the Coralie spectrograph installed in the 1.2 m Swiss Leonhard Euler Telescope at the ESO La Silla Observatory in Chile. Coralie has a spectral resolution of ≈60000 and uses a simultaneous calibration fibre illuminated by a Fabry-Perot etalon for correcting the instrumental radial-velocity drift that occurs during the science exposures. The star was observed a total of 18 times throughout the nights of 2018 Nov 15 to Nov 20. The adopted exposure time for the Coralie observations was 1200s, and the SNR obtained per resolution element at 5150 Å ranged between 50 and 60. Coralie data was processed with the CERES pipeline (Brahm et al. 2017), which performs the optimal extraction of the science and calibration fibres, the wavelength calibration and instrumental drift correction, along with the measurement of precision radial-velocities and bisector spans by using the cross-correlation technique. Specifically, a binary mask optimised for a G2-type star was used to compute the velocities for LTT 9779. The typical velocity precision achieved was ≈5 ms^{-1}, which allowed the identification the Keplerian signal with an amplitude of 20 $^{-1}$.

Table 3. Radial-velocities of LTT 9779

JD - 2450000	RV (m s^{-1})	Uncertainty (m s^{-1})	Instrument
8429.51804	-10.59	0.86	HARPS
8430.54022	-16.91	0.74	HARPS
8430.59553	-9.41	0.68	HARPS
8430.67911	1.99	0.79	HARPS
8430.76201	13.40	1.21	HARPS
8431.51068	6.71	0.61	HARPS
8431.64346	16.09	0.83	HARPS
8431.69130	14.98	0.87	HARPS
8431.73217	8.41	0.55	HARPS
8432.50941	12.77	0.73	HARPS
8432.65689	-7.23	0.94	HARPS
8432.69804	-13.45	1.06	HARPS
8432.72573	-18.32	4.02	HARPS
8464.53817	-25.17	1.02	HARPS
8464.64153	-16.81	1.11	HARPS
8464.68616	-10.08	1.27	HARPS
8465.53024	0.00	0.85	HARPS
8465.59314	10.82	0.84	HARPS
8465.64411	12.09	0.86	HARPS
8465.68104	15.61	1.12	HARPS
8466.52022	14.89	1.03	HARPS
8466.58232	8.12	0.90	HARPS
8466.63157	2.49	1.09	HARPS
8466.66865	-2.85	1.10	HARPS
8481.53213	14.93	0.94	HARPS
8481.57805	12.72	0.84	HARPS
8482.53643	-8.75	0.74	HARPS
8482.57255	-11.89	0.82	HARPS
8482.60140	-16.09	0.90	HARPS
8483.52686	-24.82	0.80	HARPS
8483.59338	-20.68	1.12	HARPS
8483.61557	-18.95	0.93	HARPS
8438.56440	-14.80	4.50	CORALIE
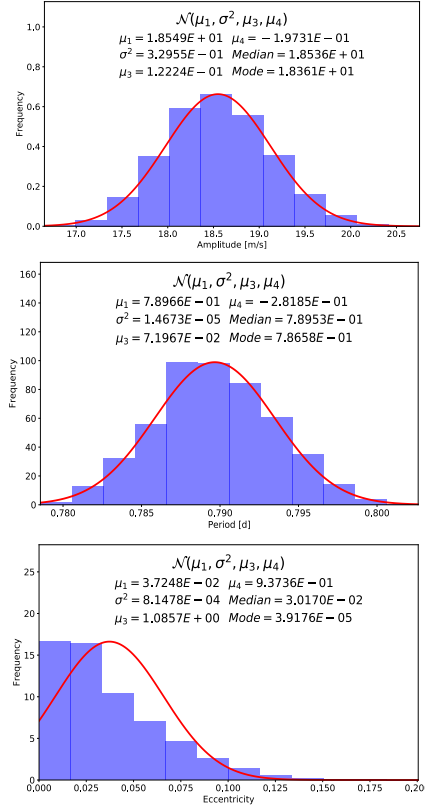
Figure 6. Independently constrained system parameters from the EMPEROR MCMC runs of the 31 HARPS radial-velocities. From top to bottom we show the posteriors of the velocity amplitude, the orbital period, and the eccentricity of the orbit. Overplotted on each histogram is a gaussian distribution with the same input parameters as those calculated from the posterior distributions. We also show the values obtained from the distributions. The histograms reveal that the signal is well constrained with the current data in hand, and the period in particular is in excellent agreement with that from the *TESS* lightcurve.

8438.62857	-7.40	4.60	CORALIE
8438.72084	10.40	5.00	CORALIE
8439.56828	35.30	5.60	CORALIE
8439.64481	3.80	4.80	CORALIE
8439.70910	-11.70	5.20	CORALIE
8440.56824	4.90	4.70	CORALIE
8440.64498	-13.20	4.70	CORALIE
8440.70927	-27.70	5.00	CORALIE
8441.57027	-16.30	4.20	CORALIE
8441.66132	-17.50	4.60	CORALIE
8441.74898	1.00	4.50	CORALIE
8442.56932	-0.60	4.50	CORALIE
8442.64202	11.60	4.90	CORALIE
8442.70651	0.60	5.00	CORALIE
8443.57400	20.10	5.00	CORALIE
8443.64711	-0.70	4.70	CORALIE
8443.71686	5.60	4.80	CORALIE

Follow-up High-angular Resolution Imaging
  NIRC2 at Keck
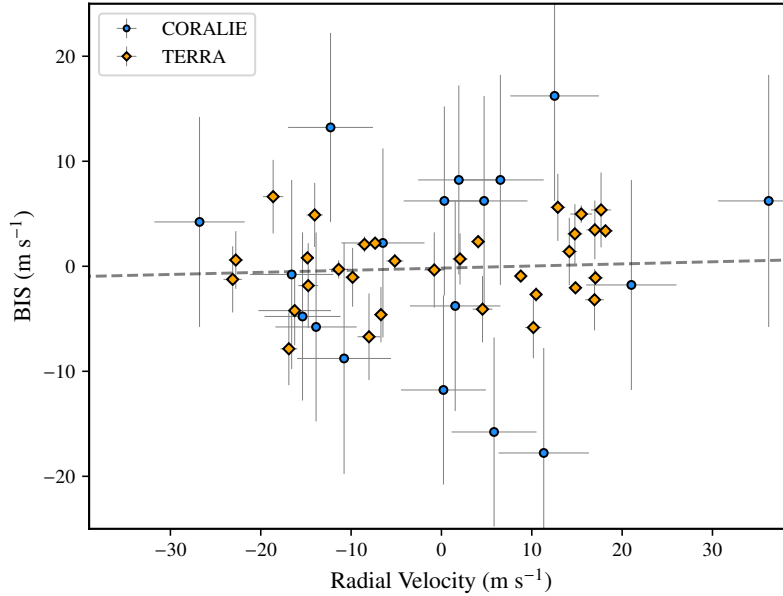
Figure 7. Spectral line bisector inverse slope measurements as a function of the radial-velocities. The orange diamonds and blue circles relate to measurements made using HARPS and Coralie, respectively. The best fit linear trend is shown by the dashed line, and a key in the upper left indicates the origin of the data points.

As part of our standard process for validating transiting exoplanets, we observed LTT 9779 with infrared high-resolution adaptive optics (AO) imaging at Keck Observatory (Ciardi et al. 2015). The Keck Observatory observations were made with the NIRC2 instrument on Keck-II behind the natural guide star AO system. The observations were made on UT 2018 Nov 22 following the standard 3-point dither pattern that is used with NIRC2 to avoid the left lower quadrant of the detector which is typically noisier than the other three quadrants. The dither pattern step size was 3″ and was repeated twice, with each dither offset from the previous one by 0.5″.

The observations were made in the narrow-band $Br-\gamma$ filter ($\lambda_o = 2.1686$; $\Delta\lambda = 0.0326\mu$m) with an integration time of 2 seconds with one coadd per frame for a total of 18 seconds on target. The camera was in the narrow-angle mode with a full field of view of $\sim 10''$ and a pixel scale of approximately $0.0099442''$ per pixel. The Keck AO observations show no additional stellar companions were detected to within a resolution $\sim 0.056''$ FWHM (Figure 8 left).

The sensitivities of the final combined AO image were determined by injecting simulated sources azimuthally around the primary target every 45° at separations of integer multiples of the central source's FWHM (Furlan et al. 2017). The brightness of each injected source was scaled until standard aperture photometry detected it with 5σ significance. The resulting brightness of the injected sources relative to the target set the contrast limits at that injection location. The final 5σ limit at each separation was determined from the average of all of the determined limits at that separation and the uncertainty on the limit was set by the rms dispersion of the azimuthal slices at a given radial distance. The sensitivity curve is shown in the left panel of Figure 8, along with an inset image zoomed to primary target showing no other companion stars.

HRCam at SOAR

In addition to the Keck observations, we also searched for nearby sources to LTT 9779 with SOuthern Astrophysical Research (SOAR) speckle imaging on 21 December 2018 UT, using the high resolution camera (HRCam) imager. Observations were performed in the I-band, which is a similar visible bandpass to that of *TESS*. Observations consisted of 400 frames, consisting of a 200×200 binned pixels region of interest, centered on the star. Each individual frame is 6.3″ on a side, with a pixel scale of 0.01575″ and 2×2 binning, with an observation time of ∼11 s, and using an Andor iXon-888 camera. More details of the observations and processing are available in Ziegler et al. (2020).

The 5σ contrast curve and speckle auto-correlation function image are shown in the right panel of Figure 8. No nearby sources were detected within 3″of LTT 9779, down to a contrast limit of 6−7 magnitudes in the I-band. We can also rule out brighter background blends very close to the star, down to around 0.1″ separation. Combining the
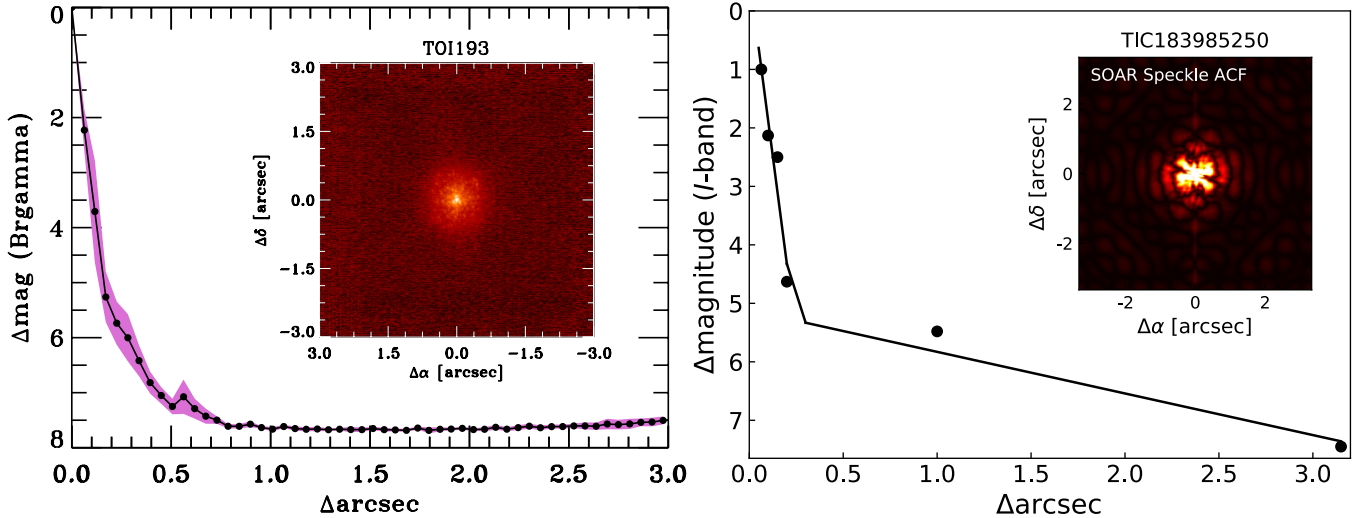
Figure 8. Companion sensitivity for the Keck NIRC2 adaptive optics imaging and the SOAR Adaptive Optics Module (SAM). For NIRC2 (left), the black points represent the 5σ limits and are separated in steps of 1 FWHM ($\sim 0.05''$); the purple represents the azimuthal dispersion (1σ) of the contrast determinations (see text). The inset image is of the primary target showing no additional companions within $3''$ of the target. For SAM (right) the black curve also represents the 5σ limit, and the black data points mark the sampling. The inset also shows the speckle image of the star, constructed from the Auto-Correlation Function.

results from Keck and SOAR, we can be rule out background blended eclipsing binaries contaminating the *TESS* large aperture used to build the LTT 9779 light curve.

Stellar Parameters

To calculate the stellar parameters for LTT 9779 we used four different methods, with three of them applied to the three different sets of spectra we obtained from NRES, TRES, and HARPS, and a photometric method that used our new tool `ARIADNE`. For the NRES spectra, we used the combination of SpecMatch and Gaia DR2 to perform the spectral classification, following the procedures explained in Fulton & Petigura (2018). TRES spectral observations used the Spectral Parameter Classification (`SPC`; Buchhave et al. 2012) tool to calculate the stellar parameters, whereas we used the Spectroscopic Parameters and atmosphEric ChemIstriEs of Stars (`SPECIES`; Soto & Jenkins 2018) and the Zonal Atmospheric Stellar Parameters Estimator (`ZASPE`; Brahm et al. 2017) algorithms to analyse the HARPS spectra. Details of these methods can be found in each of the listed publications, yet in brief, `SPC` and `ZASPE` calculate the parameters by comparing the spectra to Kurucz synthetic model grids (Kurucz 1992), either by direct spectral fitting, or by cross correlation. In this way, regions of the spectra that are sensitive to changes in stellar parameters can allow parameters to be estimated by searching for the best matching spectral model.

On the other hand, `SPECIES` uses an automatic approach to calculate equivalent widths for large numbers of atomic spectral lines of interest, Fe I for instance. The code then calculates the radiative transfer equation using `MOOG` (Sneden 1973), applying ATLAS9 model atmospheres (Castelli & Kurucz 2004), and converges on the stellar parameters using an iterative line rejection procedure. Convergence is reached once the constraints of having no statistical trend between abundances calculated from Fe I and Fe II for example, reaches a pre-determined threshold value.

Each of these three methods return consistent results for the majority of the bulk parameters, in particular the stellar effective temperature is in excellent agreement, with a mean value of 5480 ± 42 K, along with the surface gravity

($\log g$) of the star, which is found to be 4.47±0.11 dex. For the metallicity of the star, all three methods find the star to be metal-rich, with a mean value of +0.27±0.04 dex. For the main parameters of interest in this work, the stellar mass and radius, we used two different methods, with the mass value coming from the combination of the GAIA DR2 parallax for the star (Gaia Collaboration et al. 2016, 2018), along with either the MESA Isochrones and Stellar Tracks (MIST; Dotter 2016) models, or the Yonsei-Yale (YY; Yi et al. 2001) isochrones, and we find a value of $1.02^{+0.02}_{-0.03}$ $M_\odot$.

For the radius, we used the `ARIADNE` code (Vines & Jenkins 2020), which is a new python tool designed to automatically fit stellar spectral energy distributions in a Bayesian Model Averaging framework. We convolved Phoenix v2 (Husser et al. 2013), BT-Settl, BT-Cond (Allard et al. 2012), BT-NextGen (Hauschildt et al. 1999; Allard et al. 2012), Castelli & Kurucz (2004), and Kurucz (1993) model grids with commonly available filter bandpasses: UBVRI; 2MASS JHK_s; SDSS ugriz; ALL-WISE W1 and W2; Gaia G, RP, and BP; Pan-STARRS griwyz; Stromgren uvby; GALEX NUV and FUV; Spitzer/IRAC 3.6μm and 4.5μm; TESS; Kepler; and NGTS creating six different model grids, which we then interpolated in Teff−log g−[Fe/H] space. ARIADNE also fits for the radius, distance, Av and excess noise terms for each photometry point used, in order to account for possible underestimated uncertainties. We used the `SPECIES` results as priors for the $T_{\rm eff}$, $\log g$, and [Fe/H], and the distance is constrained by the Gaia DR2 parallax, after correcting it by the offset found by Stassun & Torres (2018). The radius has a prior based on GAIAs radius estimate and the Av has a flat prior limited to 0.029, as per the re-calibrated SFD galaxy dust map (Schlegel et al. 1998; Schlafly & Finkbeiner 2011). We performed the fit using dynestys nested sampler (Speagle 2020), which returns the Bayesian evidence of each model, and then afterwards we averaged each model posterior samples weighted by their respective normalized evidence. This returned a final stellar radius of 0.949±0.006 $R_\odot$.

As LTT 9779 b appears as an odd-ball when scrutinising its mass and radius, we want to be sure that the stellar radius is not biased in the sense that the star is really an evolved star, much larger than the stellar modelling predicts, and hence the planet is more likely a UHJ. Although we have arrived at the same values from three different analyses and instrumental data sets, we can add more confidence to the results by studying the stellar density throughout the MCMC modelling process, when assuming the planet's orbit is circular. In this case, we place a log-uniform prior on the stellar density, constrained to be within 100−10'000 kgm^{-3}, and then study how it changes as a function of $R_p/R_\star$.

We find that the distribution is bimodal (Figure 9), with the most likely stellar density region given by the lower, more densely constrained part of the parameter space in the figure. The upper mode in the figure, pushing towards higher stellar densities and lower values of $R_p/R_\star$, is arguing towards the star being an M dwarf, which is ruled out by the high resolution spectroscopic data, and is inconsistent with our global-modelling effort (less probable part of the posterior space). This mode is also only consistent with a very narrow set of limb-darkening coefficients, all of which are inconsistent at several sigma with theoretical models, whereas the lower, more probable mode, has a wide range of possible limb-darkening coefficients, which are all in agreement with theoretical models. Therefore, this test rules out a more evolved state for the star in either case, with the higher probability mode being in excellent agreement with the results from the stellar modelling.

Finally, for the confirmation of the transit and radial-velocity parameters it is prudent to analyse the activity of the star, in order to assess the impact that any activity could have on the measurements. From the above analyses we find the star to be a very slow rotator, with a HARPS $v \sin i$ limit of 1.06±0.37 km s^{-1}, lower than the projected solar $v \sin i$ value (1.6±0.3 km s^{-1}) determined from HARPS spectral analysis (Pavlenko et al. 2012), indicating a slowly rotating, and therefore inactive star. Given the calculated radius of the star, such a slow rotation gives rise to an upper limit of the rotation period to be 45 d. If the planetary orbit is aligned with the stellar plane of rotation, such that we can assume the inclination angle is the same, then this value is the absolute rotation period. Kepler Space Telescope data analysis of old field stars of this spectral type, have rotation periods ranging from a few days for the youngest stars, with a peak around 20 d, and a sharp fall after this with a tail reaching up to almost 100 d (McQuillan et al. 2014). A rotation period of 45 d would place LTT 9779 in the upper tail of the Kepler distribution, indicating the star is old, and agreeing with the combined age estimate of $2.0^{+1.3}_{-0.9}$ Gyrs. This result would also suggest that the activity of the star should be weak. We calculate the activity using the Ca II HK lines, following the analysis procedures and methods presented in Jenkins et al. (2006, 2008, 2011, 2017). We find the star to be inactive, with a HARPS S-index of 0.148±0.008, which relates to a mean $logR'_{HK,HARPS}$ of -5.10±0.04 dex. Gyrochronology relations (Mamajek & Hillenbrand 2008) would therefore suggest an age closer to ∼5 Gyrs or so, again confirming that the star should not be young. Taken all together, LTT 9779 can be classed as an inactive and metal-rich solar analogue star, and all key
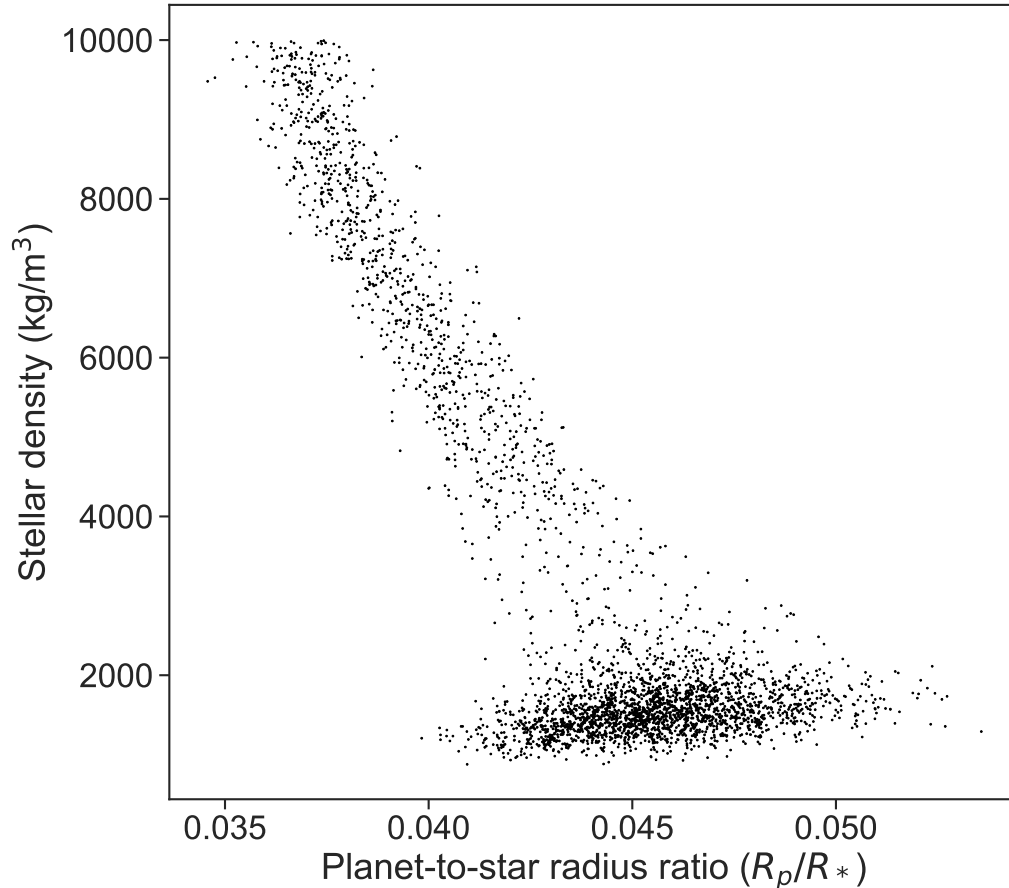
Figure 9. Stellar density as a function of $R_p/R_\star$ when modelling the *TESS* light curve with a log-uniform prior on the stellar density and the planetary eccentricity constrained to be zero.

properties can be found in Table 1.

Global Modelling

As stated in the main text, the global modeling of the data was performed using `juliet` (Espinoza et al. 2019). This code uses `batman` (Kreidberg 2015) to model the transit lightcurves and `radvel` (Fulton et al. 2018) to model the radial-velocities. We performed the posterior sampling using MultiNest (Feroz et al. 2009) via the PyMultiNest wrapper (Buchner et al. 2014).

The fit was parameterized by the parameters r_1 and r_2, both having uniform distributions between 0 and 1, which are transformations of the planet-to-star radius ratio p and impact parameter b that allow an efficient exploration of the parameter space (Espinoza 2018). In addition, we fitted for the stellar density by assuming a prior given by the value obtained with our analysis of the stellar properties, assuming a normal prior for this parameter with a mean of 1810 kg/m^3 and standard deviation of 130 kg/m^3. We parameterized the limb-darkening effect using a quadratic law defined by parameters u_1 and u_2; however, we use an uninformative parameterization scheme (Kipping 2013) in which we fit for $q_1 = (u_1 + u_2)^2$ and $q_2 = u_1/(2u_1 + 2u_2)$ with q_1 and q_2 having uniform priors between 0 and 1. For the radial-velocity parameters, we used wide priors for both the systemic radial-velocity of each instrument and the possible jitter terms, added in quadrature to the data.

For the photometry, we considered unitary dilution factors for the *TESS* NGTS and LCOGT photometry after leaving them as free parameters and observing that it was not needed based on the posterior evidence of the fits. This is consistent with the a-priori knowledge that the only source detected by Gaia DR2 within the *TESS* aperture is a couple of faint sources to the south-east of the target, the brighter of which has $\Delta G = 5.4$ with the target. If

we assume the Gaia passband to be similar to the *TESS* passband, this would imply a dilution factor $D > 0.99$, which is negligible for our purposes. For the *TESS* photometry, no extra noise model nor jitter term was needed to be added according to the bayesian evidence of fits incorporating those extra terms. For the NGTS observations, we considered the data of the target from the nine different telescopes as independent photometric datasets (i.e., having independent out-of-transit baseline fluxes in the joint fit), that share the same limb-darkening coefficients. We initially added photometric jitter terms to all the NGTS observations, but found that fits without them for all instruments were preferred by looking at the bayesian evidences of both fits. For the LCOGT data, we used gaussian process in time to detrend a smooth trend observed in the data. A kernel which was a product of an exponential and a matern 3/2 was used, and a jitter term was also fitted and added in quadrature to the reported uncertainties in the data — this was the model that showed the largest bayesian evidence. We note that fitting the lightcurves independently provides statistically similar transit depths to the joint model, showing that all are in statistical agreement. Finally, an eccentric orbit is ruled out by our data with an odds ratio of 49:1 in favor of a circular orbit; the eccentric fit, performed by parameterizing the eccentricity and argument of periastron via $\mathcal{S}_1 = \sqrt{e}\cos\omega$ and $\mathcal{S}_2 = \sqrt{e}\sin\omega$, gives an eccentricity given our data of $e < 0.058$ with a 95% credibility.

With all the photometry in hand, we could also compare individually each light curve transit model to test if they are in statistical agreement, or any biases exist, such that the radius measurement is biased. We proceeded to again fit each light curve independently with `juliet`, recording the transit model depths to test for statistical differences. As expected, we found the *TESS* photometry produced the most precise value ($T_{d,TESS} = 2299^{+320}_{-240}$ ppm), with the LCO and NGTS fits arriving at values of $T_{d,LCO} = 1925^{+620}_{-400}$ ppm and 1594^{+980}_{-715} ppm, respectively. All three are in statistical agreement. We also jointly modeled the LCO and NGTS lightcurves to provide a more constrained comparison with the *TESS* photometry, and found a value of $T_{d,LCO+NGTS} = 1678^{+540}_{-290}$ ppm, again in statistical agreement with the *TESS* value. Therefore, we can be confident that all three instruments provide a similar description for the planet's physical size.

Transit Timing Variations

The Transit Timing Variations (TTVs) of LTT 9779 b was measured using the `EXOFASTv2` (Eastman et al. 2013; Eastman 2017) code. `EXOFASTv2` uses the Differential Evolution Markov chain Monte Carlo method (DE-MC) to derive the values and their uncertainties of the stellar, orbital and physical parameters of the system. For the TTV analysis of LTT 9779 b we fixed the stellar and orbital parameters to the values obtained from the global fit performed by `SPECIES` and `juliet`, except for the transit time of each light curve and their baseline flux.

In a Keplerian orbit, the transit time of an exoplanet follows a linear function of the transit epoch number (E):

$$T_c(E) = T_c(0) + PE \tag{1}$$

Where P is the orbital period of the exoplanet and $T_c(0)$ is the optimal transit time in a arbitrary zero epoch and corresponds to the time that is least covariant with the period and has the smallest uncertainty. Our best-fitted value from `EXOFASTv2` is: $T_c(0) = 2458354.2145 \pm 0.0012$ BJD.

All the transit times were allowed to move from the linear ephemeris and each one was considered as one independent TTV parameter in the `EXOFASTv2`'s fitting, resulting in 33 parameters to fit. The best fit results are shown in Figure 10, where the grey area corresponds to the 1σ of the linear ephemeris shown in Equation (1).

We found no evidence of a clear periodic variation in the transit time. The RMS variation from the linear ephemeris is $\sigma = 181.8$ sec. There are only two values above the 2σ limit, if we remove them the RMS deviation is reduced to 155.9 sec. On the other hand, the reduced chi-squared is $\chi^2_{red} = 1.23$, which is an indicator that the transit times fit accordingly with the proposed linear ephemeris.

In conclusion, the existence of transit timing variations in LTT 9779 b is not evident for the time-span of our transit data. In addition, with the apparent lack of another short period signal in the RV data, this suggest that there is no other inner companion in the planetary system. Any other tertiary companion must be far from LTT 9779 b, such that the gravitation or tidal interactions are small, and the linear trend in the RVs might be pointing in that direction.

Metallicity Analysis

The correlation between the presence of giant planets and host star metallicity has been well established (Gonzalez 1997; Fischer & Valenti 2005; Jenkins et al. 2017; Maldonado et al. 2018), along with the apparent lack of any correlation for smaller planets (Jenkins et al. 2013; Buchhave et al. 2012, 2014). We studied the small sample of known USP
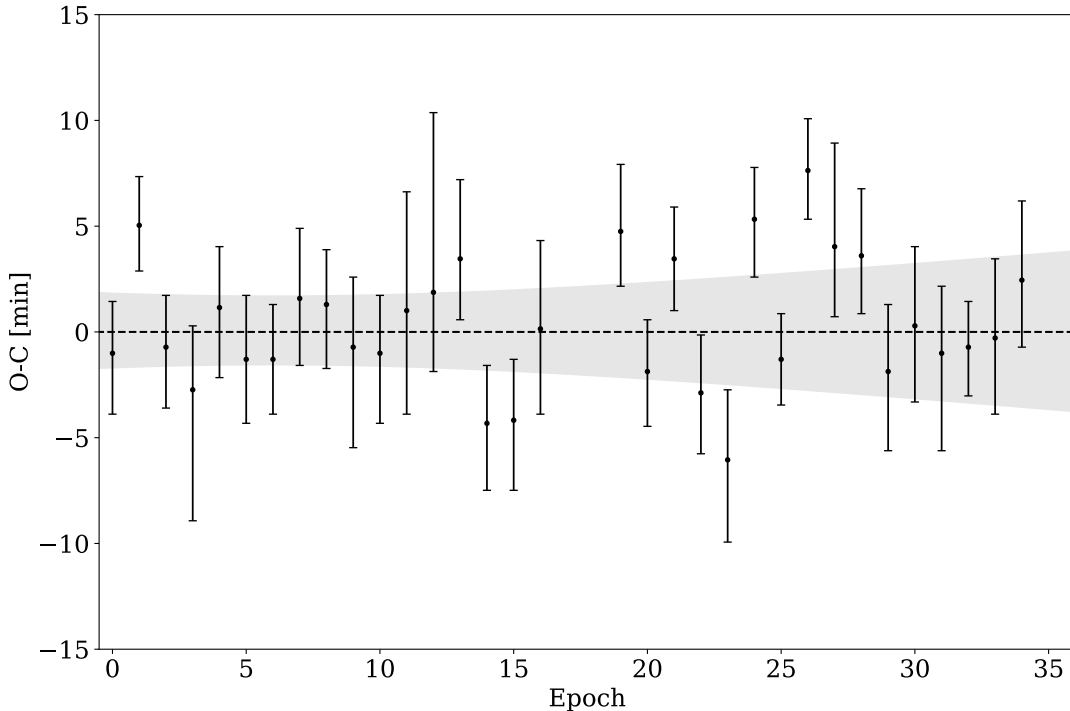
Figure 10. Observed minus computed mid-transit times of LTT 9779 b. The residuals (TTV) of the transit times are shown considering the proposed linear ephemeris. The dashed line corresponds to zero variation and the grey area is the propagation of 1σ uncertainties, considering the optimal transit time from `EXOFASTv2` and the period from `juliet`. The epoch 0 is the first light curve obtained by *TESS* and is also the corresponding epoch of the optimal transit time. The TTV values shown in this plot fit accordingly with the proposed linear ephemeris ($\chi^2_{red} = 1.23$).

planets and Ultra Hot Jupiters (UHJs, the gas giant planets with orbit periods of less than 1 day), using values taken from the TEPCat database (Southworth 2011), whilst recalculating metallicities for those where we could find their spectra, (~half the sample), using `SPECIES` (Soto & Jenkins). We found a similar general trend, whereby the USP planets tend to orbit more metal-poor stars when compared with the UHJs, however the sample is small enough that single outliers bias the statistics, therefore we extended slightly the orbital period selection out to 1.3 days, increasing the sample by over 55%. With this updated sample, we find a Kolmogorov-Smirnov (KS) test probability of only 1% that the USP planets and UHJs are drawn from the same parent population.

A couple of notable exceptions to the trend here are the planets 55 Cancri e and WASP-47 e, both small USP planets that orbit very metal-rich stars. However, there exists additional gas giant planets in these systems, meaning they still follow the overall picture. If we exclude these two, the KS probability drops to 0.1% that the populations are statistically similar. The diversity of USP planets is high, therefore many more detections are needed to statistically constrain the populations in this respect. We also require more UHJs to build up a statistical sample, since the subsolar metallicity of WASP-43 can also bias the tests. If we look at the density-metallicity parameter space (Figure 4), there are indications of a general trend whereby the low-density planets are mostly UHJs orbiting metal-rich stars, and the higher density USP planets orbit more metal-poor stars.

3.7. Data availability

Photometric data that support the findings of this study are publically available from the Mikulski Archive for Space Telescopes (MAST; http://archive.stsci.edu/) under the TESS Mission link. All radial-velocity data re available from the corresponding author upon reasonable request. Raw and processed spectra can be obtained from the European Southern Observatorys data archive at http://archive.eso.org.

3.8. Code Availability

All codes necessary for the reproduction of this work are publically available through the GitHub repository, as follows:

EMPEROR: https://github.com/ReddTea/astroEMPEROR
Juliet: https://github.com/nespinoza/juliet
SPECIES: https://github.com/msotov/SPECIES
ARIADNE: https://www.github.com/jvines/astroARIADNE
CERES: https://github.com/rabrahm/ceres
ZASPE https://github.com/rabrahm/zaspe

<div align="center">REFERENCES</div>

Allard F., Homeier D., Freytag B., 2012, Philosophical Transactions of the Royal Society of London Series A, 370, 2765

Anglada-Escudé G., Butler R. P., 2012, ApJS, 200, 15

Benedict G. F. et al., 2016, AJ, 152, 141

Brahm R., Jordán A., Espinoza N., 2017, PASP, 129, 034002

Brahm R., Jordán A., Hartman J., Bakos G., 2017, MNRAS, 467, 971

Brown T. M. et al., 2013, PASP, 125, 1031

Buchhave L. A. et al., 2010, ApJ, 720, 1118

Buchhave L. A. et al., 2014, Nature, 509, 593

Buchhave L. A. et al., 2012, Nature, 486, 375

Buchner J. et al., 2014, A&A, 564, A125

Casasayas-Barris N. et al., 2019, A&A, 628, A9

Castelli F., Kurucz R. L., 2004, xxx, 1

Chadney J. M., Galand M., Unruh Y. C., Koskinen T. T., Sanz-Forcada J., 2015, Icarus, 250, 357

Ciardi D. R., Beichman C. A., Horch E. P., Howell S. B., 2015, ApJ, 805, 16

Dotter A., 2016, ApJS, 222, 8

Eastman J., , 2017, EXOFASTv2: Generalized publication-quality exoplanet modeling code

Eastman J., Gaudi B. S., Agol E., 2013, Publications of the Astronomical Society of the Pacific, 125, 83

Ehrenreich D. et al., 2015, Nature, 522, 459

Espinoza N., 2018, Research Notes of the American Astronomical Society, 2, 209

Espinoza N., Kossakowski D., Brahm R., 2019, MNRAS, 490, 2262

Feroz F., Hobson M. P., Bridges M., 2009, MNRAS, 398, 1601

Főrész G., Szentgyorgyi A. H., Meibom S., 2008, in Santos N. C., Pasquini L., Correia A. C. M., Romaniello M., eds, Precision Spectroscopy in Astrophysics. pp 287–290

Fischer D. A., Valenti J., 2005, ApJ, 622, 1102

Fressin F. et al., 2013, ApJ, 766, 81

Fulton B. J., Petigura E. A., 2018, AJ, 156, 264

Fulton B. J., Petigura E. A., Blunt S., Sinukoff E., 2018, PASP, 130, 044504

Furlan E. et al., 2017, AJ, 153, 71

Gaia Collaboration et al., 2018, A&A, 616, A1

Gaia Collaboration et al., 2016, A&A, 595, A1

Gonzalez G., 1997, MNRAS, 285, 403

Hauschildt P. H., Allard F., Baron E., 1999, ApJ, 512, 377

Horne K., 1986, PASP, 98, 609

Husser T. O., Wende-von Berg S., Dreizler S., Homeier D., Reiners A., Barman T., Hauschildt P. H., 2013, A&A, 553, A6

Ionov D. E., Pavlyuchenkov Y. N., Shematovich V. I., 2018, MNRAS, 476, 5639

Jackson A. P., Davis T. A., Wheatley P. J., 2012, MNRAS, 422, 2024

Jenkins J. M. et al., 2016, in Software and Cyberinfrastructure for Astronomy IV. p. 99133E

Jenkins J. S., Jones H. R. A., Pavlenko Y., Pinfield D. J., Barnes J. R., Lyubchik Y., 2008, A&A, 485, 571

Jenkins J. S. et al., 2006, MNRAS, 372, 163

Jenkins J. S., Jones H. R. A., Tuomi M., Díaz M., Cordero J. P., Aguayo A., et al. 2017, MNRAS, 466, 443

Jenkins J. S. et al., 2013, ApJ, 766, 67

Jenkins J. S. et al., 2011, A&A, 531, A8

King G. W. et al., 2018, MNRAS, 478, 1193

Kipping D. M., 2013, MNRAS, 435, 2152

Kreidberg L., 2015, Publications of the Astronomical Society of the Pacific, 127, 1161

Kubyshkina D. et al., 2018, A&A, 619, A151

Kurucz R., 1993, ATLAS9 Stellar Atmosphere Programs and 2 km/s grid. Kurucz CD-ROM No. 13. Cambridge, 13

Kurucz R. L., 1992, in Barbuy B., Renzini A., eds, IAU Symposium Vol. 149, The Stellar Populations of Galaxies. p. 225

Li J., Tenenbaum P., Twicken J. D., Burke C. J., Jenkins J. M., Quintana E. V., Rowe J. F., Seader S. E., 2019, PASP, 131, 024506

Lindegren L. et al., 2018, A&A, 616, A2

Lindegren L. et al., 2016, A&A, 595, A4

Lindegren L., Lammers U., Hobbs D., O'Mullane W., Bastian U., Hernández J., 2012, A&A, 538, A78

Lopez E. D., 2017, MNRAS, 472, 245

Lopez E. D., Fortney J. J., 2014, ApJ, 792, 1

Lundkvist M. S. et al., 2016, Nature Communications, 7, 11201

Maldonado J., Villaver E., Eiroa C., 2018, A&A, 612, A93

Mamajek E. E., Hillenbrand L. A., 2008, ApJ, 687, 1264

Mazeh T., Holczer T., Faigler S., 2016, A&A, 589, A75

McCormac J., Pollacco D., Skillen I., Faedi F., Todd I., Watson C. A., 2013, PASP, 125, 548

McQuillan A., Mazeh T., Aigrain S., 2014, ApJS, 211, 24

Méndez A., Rivera-Valentín E. G., 2017, ApJL, 837, L1

Michalik D., Lindegren L., Hobbs D., Lammers U., 2014, A&A, 571, A85

Nortmann L. et al., 2018, Science, 362, 1388

Owen J. E., Jackson A. P., 2012, MNRAS, 425, 2931

Owen J. E., Wu Y., 2017, ApJ, 847, 29

Pavlenko Y. V., Jenkins J. S., Jones H. R. A., Ivanyuk O., Pinfield D. J., 2012, MNRAS, 422, 542

Peña Rojas P. A., Jenkins J. S., 2020, A&A, p. in prep

Pepe F. et al., 2000, in Iye M., Moorwood A. F., eds, SPIE Vol. 4008, Optical and IR Telescope Instrumentation and Detectors. pp 582–592

Raghavan D. et al., 2010, ApJS, 190, 1

Rey J. et al., 2017, A&A, 601, A9

Ricker G. R. et al., 2015, Journal of Astronomical Telescopes, Instruments, and Systems, 1, 014003

Robin A. C., Reylé C., Derrière S., Picaud S., 2003, A&A, 409, 523

Sanchis-Ojeda R., Rappaport S., Winn J. N., Kotson M. C., Levine A., El Mellah I., 2014, ApJ, 787, 47

Schlafly E. F., Finkbeiner D. P., 2011, ApJ, 737, 103

Schlegel D. J., Finkbeiner D. P., Davis M., 1998, ApJ, 500, 525

Siverd R. J. et al., 2018, in Ground-based and Airborne Instrumentation for Astronomy VII. p. 107026C

Smith A. M. S. et al., 2020, Exp. Astron, submitted

Smith J. C. et al., 2012, PASP, 124, 1000

Sneden C. A., 1973, PhD thesis, THE UNIVERSITY OF TEXAS AT AUSTIN.

Soto M. G., Jenkins J. S., 2018, A&A, 615, A76

Southworth J., 2011, MNRAS, 417, 2166

Speagle J. S., 2020, MNRAS

Stassun K. G., Torres G., 2018, The Astronomical Journal, 862, 1

Stumpe M. C., Smith J. C., Catanzarite J. H., Van Cleve J. E., Jenkins J. M., Twicken J. D., Girouard F. R., 2014, PASP, 126, 100

Twicken J. D. et al., 2018, PASP, 130, 064502

Valsecchi F., Rappaport S., Rasio F. A., Marchant P., Rogers L. A., 2015, ApJ, 813, 101

van Leeuwen F., 2007, A&A, 474, 653

Vidal-Madjar A. et al., 2004, ApJL, 604, L69

Vines J. I., Jenkins J. S., 2020, in prep

West R. G. et al., 2019, MNRAS, 486, 5094

Wheatley P. J. et al., 2018, MNRAS, 475, 4476

Winn J. N., Sanchis-Ojeda R., Rappaport S., 2018, NewAR, 83, 37

Yi S., Demarque P., Kim Y.-C., Lee Y.-W., Ree C. H., Lejeune T., Barnes S., 2001, ApJS, 136, 417

Zechmeister M., Kürster M., 2009, A&A, 496, 577

Zeng L., Sasselov D. D., Jacobsen S. B., 2016, ApJ, 819, 127

Ziegler C., Tokovinin A., Briceño C., Mang J., Law N., Mann A. W., 2020, AJ, 159, 19